Universidad de Concepción
Dirección de Postgrado
Facultad de Ciencias Químicas
Programa Doctorado en Ciencias Geológicas

# Deformación cortical intersísmica en zonas de subducción: Validando el modelo conceptual de subducción en el margen Chileno

Tesis para optar al grado de Doctor en Ciencias Geológicas

MARCELO ANDRES CONTRERAS KOHL

CONCEPCIÓN-CHILE
2019

Profesor Guía: Andrés Tassara Oddo

Dpto. de Ciencias de la Tierra, Facultad de Ciencias Químicas
Universidad de Concepción

## Agradecimientos

Quiero expresar mis agradecimientos por proporcionar apoyo y financiamiento en las distintas etapas del desarrollo de esta tesis. A Muriel Gerbault por sus valiosas contribuciones y estadía en Nice, Francia. A la Dirección de Postgrado de la Universidad de Concepción por su apoyo a eventos y pasantías. A los Proyectos Fondecyt 1151175 Active Tectonics and Volcanism at the Southern Andes, 1101034 Convergence Partitioning at the Southern Andes. Al Nucleo Milenio NC160025 «El ciclo sísmico a lo largo de zonas de subducción». A la ayuda de valiosas personas, a mi profesor guía Andrés Tassara por su apoyo, confianza y orientación a largo del desarrollo de esta tesis. Al Dr. Klaus Bataille quién me ha apoyado y orientado desde el pre-grado en el camino de las Ciencias de la Tierra. Al Dr. Rodolfo Araya por su particular humor, tiempo y apoyo en el fundamental desarrollo computacional de este trabajo. Al Dr. Marcos Moreno, del Deutsches GeoForschungsZentrum - Potsdam, Alemania, por amistad, apoyo, orientación y contribuciones fundamentes en este presente estudio. Agradezco también a Isabel Urrutia con quién tuve largas charlas en aspectos geológicos y apoyo durante mi pasantía en el GFZ. A Julius Jara, Rodrigo Mora y Hugo Soto, quienes compartieron sus conocimientos en variados aspectos geológicos y geofísicos muy importantes en el desarrollo de este trabajo.

Marcelo Contreras Kohl.

## Resumen

Variados modelos analíticos y numéricos de deformación apoyados en observaciones de la deformación de la corteza han sido utilizados en las últimas décadas para explorar la relación entre el ciclo sísmico de subducción y la deformación de la placa superior en el antearco Andino. Mediante el método de elementos finitos, geometrías realistas derivadas de datos geofísicos externos y observaciones superficiales relacionadas al estado actual de la deformación del antearco, se modela cinemáticamente la zona de subducción Chileno $(19 - 44^{o}S)$. Estos modelos abordan la deformación cortical intersísmica mediante la evaluación de variados parámetos de subducción relacionados a zona de contacto sismogénica, logrando reproducir las velocidades intersísmicas previas a la ocurrencia del terremoto Mw8.8 del Maule 2010. Los resultados fueron vinculados a modelos dinámicos numéricos complementarios a escalas de tiempo más largas y reología compleja para evaluar el significado mecánico de las condiciones cinemáticas que simulan la deformación intersísmica. Los resultados indican que para una zona sismogénica con alto grado de acoplamiento, los desplazamientos superficiales observados por GPS se deben a la existencia de tasas de deslizamiento no homogéneo en la base de la litósfera subductora que disipa el alto esfuerzo de flexión resultante de la interacción mecánica de la losa con el manto subyacente. Las consideraciónes e implicancias mecánicas por medio de un sencillo modelo mecánico 2D y extedido a 3D entrega un nuevo enfoque de la deformación del antearco, pudiendo reproducir sin complejidad el patrón de la deformación intersísmica a lo largo de Chile. Los desajustes entre las predicciones de nuestro modelo y las velocidades del GPS se pueden utilizar para inferir variaciones del grado de acople sismogénico. Los resultados demuestran que la geometría de la losa, tanto la flexión y la contribución continua a largo plazo de la subducción tienen un gran impacto en los desplazamientos superficiales de la deformación intersísmica, controlando el patrón principal de la tasa de desplazamiento del antearco en la zona de subducción Chilena.

## Abstract

Various analytical and numerical deformation models supported by observations of crust deformation have been used in recent decades to explore the relationship between the seismic cycle of the interplate megathrust fault and the deformation of the upper plate in the Andean forearc. Using the method of finite elements, realistic geometries derived from external geophysical data and surface observations related to the current state of the forearc deformation, the Chilean subduction zone $(19 - 44^{o}S)$. These models address interseismic crustal deformation through the evaluation of various subduction parameters related to seismogenic contact zone, managing to reproduce the interseismic velocities prior to the occurrence of the Mw8.8 Maule 2010 earthquake. The results were linked to complementary numerical dynamic models at longer timescales and complex rheology to evaluate the mechanical significance of the kinematic conditions simulating the interseismic deformation. This results show that for a seismogenic zone with a high degree of coupling, the surface displacements observed by GPS are due to the existence of non-homogeneous slip rates at the base of the slab that dissipate the resulting high bending stress due to the mechanical interaction of the slab with the underlying mantle. The mechanical considerations and implications by means of a simple mechanical model 2D and extended to 3D provides a new approach to the deformation of the forearc, being able to reproduce without complexity the pattern of interseismic deformation throughout Chile. The mismatches between the predictions of our model and the GPS velocities can be used to infer variatios of the seismogenic locking degree. The results demonstrate that slab geometry, as bending and the long-term continuous contribution of subduction have a large impact on the surface displacements of the interseismic deformation, controlling the main pattern of the forearc displacement rate in the Chilean subduction zone.

# Índice general

## Capítulo 1

# INTRODUCCIÓN GENERAL

Chile se encuentra ubicado adyacente a un margen convergente de tipo Andino, donde la placa oceánica se desliza bajo la placa continental entrando en el manto subyacente (Forsyth & Uyeda, 1975) formando cadenas montañosas y volcánicas en la placa continental. Este proceso evidencia deformaciones en la corteza continental producida en su mayor parte por la acumulación y liberación de energía elástica, debido a la recurrencia de grandes terremotos en intervalos de tiempo que van desde décadas hasta varios siglos de duración. El período de tiempo transcurrido entre la ocurrencia de dos grandes terremotos localizados en una porción del espacio de la zona de contacto sismogénica, define un ciclo sísmico de subducción. Dentro de un ciclo se distingue la fase intersísmica, esta involucra un período prolongado de tiempo durante el cual existe acumulación de deformación elástica a lo largo de la mega-falla mientras se encuentra total o parcialmente bloqueada, transmitiendo desplazamientos hacia la superficie de la placa continental. La condición de bloqueo parcial o total de la mega-falla obedece a condiciones dinámicas durante el proceso de subducción, las que provocan que la zona de contacto pueda permanecer en una gama de estados friccionales estables o inestables acuerdo a diferentes leyes constitutivas (Scholz, 1998). Si las condiciones mecánicas en la zona de bloqueo permiten que la tensión alcancen un umbral crítico, la fase cosísmica comienza y se libera la deformación elástica acumulada durante el intersísmico en un proceso de ruptura de roca que dura pocos segundos o minutos, provocando que todos los desplazamientos finalmente alcanzan la tasa de deslizamiento

de campo lejano. Seguido al co-sísmico, se da inicio a la fase post-sísmica. Esta fase puede tener asiciada distintos fenomenos a escalas variables en tiempo y espacio; after slip, en el cual la falla continua deslizándose hacia el océano, luego la relajación viscoelástica inducida por la relajación del manto superior y finalmente las condiciones mecánicas restablecen el re-acoplamiento de la mega falla de subducción dando paso a un nuevo ciclo de subducción (Wang *et al.* , 2012).

El acoplamiento interplaca durante la fase intersísmica es responsable de grandes terremotos y ha sido estudiada mayormente de una manera puramente cinemática, por medio de observaciones geodéticas junto con modelos de dislocación elástica tanto numéricos como analíticos (Savage, 1983; Okada, 1992). Este tipo de modelos predicen el estado de bloqueo o deslizamiento de la falla independiente del mecanismo de carga y las propiedades de fricción (e.g., Dragert *et al.* , 2001). Modelos mas recientes incorporan restricciones cinemáticas desde la geodesia satelital, con observaciones aportadas desde densos arreglos de estaciones de GPS (e.g., Larson et al., 2003). Otros estudios mediante el método de elementos finitos, incorporan características físicas más complejas, como las variaciones reológicas viscoelásticas para estudiar las variaciones espaciales de la deformación intersísmica (Wang *et al.* , 2003; Hyodo & Hirahara, 2003).

Variados son los parámetros de subducción (Jarrard, 1986) relacionados a la deformación de antearcos y el comportamiento interplaca que intentan explicar la deformación elástica intersísmica a través de distintos modelos de subducción basandose en consideraciones tanto geométricas, mecánicas y tectónicas, las que pueden conducir a distintas implicancias en nuestro entendimiento respecto de acople interplaca. Dos son los modelos de dislocación elástica mas utilizados, el propuesto originalmente por Savage (1983) y las soluciones analíticas de Okada (1985). Ambos han sido utilizados para interpretar cinemátimente el ciclo sísmico completo incorporando dislocaciones en geometrías de tierra bidimensionales idealizadas atribuyéndoles diferentes propiedades reológicas o composicionales, tales como semiespacios elásticos infinitos

o litósfera elástica sobre astenósfera viscoelástica (Thatcher & Rundle, 1984; Cohen, 1994). Sin embargo, utilizar una simple interface para describir cinemáticamente la deformación intersísmica durante la subducción, no puede proporcionar correctamente conocimientos sobre los procesos físicos y mecánicos que tienen lugar en las zonas de subducción. Back Slip Model (BSM) asume que el megaempuje es una falla finita incrustada en un medio elástico y simula el período intersísmico mediante un deslizamiento de una falla normal a la velocidad de convergencia. Modelos cinemáticos como estos, que excluyen la presencia de la placa en subducción tal como el Back Slip Model (Savage, 1983), no predice correctamente el estado de stress asociado con el acople de placas (Douglass & Buffeft, 1995).

La inclusión del espesor del Slab en modelos geométricos de subducción sintetizados, imponiendo condiciones cinemáticas y mecánica de acoplamiento interplaca, son mas consistentes con el modelo conceptual de subducción, ya que pueden reproducir correctamente la deformación superficial y el patrón principal de concentración de esfuerzos asociados con el acoplamiento de placas en una zona de subducción (Zhao & Takemoto, 2000). Kanda y Simons (2010) incluye los efectos cinemáticos de la flexión del Slab proporcionando mayor comprensión del proceso de flexura de la placa . Además, demuestran que la solución del Back Slip Model (BSM) es idéntica a la solución del Elastic Subduction Plate Model (ESPM) cuando el espesor de la placa es insignificante y por lo tanto el Back Slip Model es un caso extremo del ESPM.

Desde un punto de vista cinemático y escala del ciclo sísmico nacen algunas interrogantes ¿Cómo un modelo de subducción puede reproducir la deformación intersismica mediante el modelo de dislocación elástica en semiespacios infinitos? ¿Qué parámetros de subducción influyen en la deformación cortical intersísmica ? ¿Tiene algún rol la flexura de la placa subductada en el grado de acople interplaca? ¿Existe alguna contribución de largo plazo de la placa en subducción a escala de la fase intersísmica?.

## 1.1. Hipótesis

Según lo expuesto anteriormente, la deformación cortical en zonas de subducción está vinculada a los procesos de la flexión de la placa elástica en subducción e interacción mecánica con el manto subyacente a lo largo de la base de la placa subductora. Develar qué procesos se llevan a cabo en la base del Slab y manto-oceánico en la zona de flexura, aportarán a una mejor comprensión y cuantificación del acople mecánico interplaca así como el comportamiento friccional de la mega-falla de subducción durante la fase intersísmica.

## 1.2. Objetivos

### 1.2.1. Objetivo General

En el marco del estado actual de la zona en estudio y la escala del ciclo sísmico, se pretende abordar los procesos que afectan la deformación cortical en los Andes Centrales y del Sur, caracterizando detalladamente las estructuras mecánicas y reológicas mediante un modelo numérico en dos y tres dimensiones, que incorpore información sobre la zona de subducción en términos de su geometría, reología y campo de deformación actual del antearco.

### 1.2.2. Objetivos Específicos

1. Implementar un modelo numérico mecánico en 2D y 3D dimensiones que incorpore la reología y geometría de zona de subducción a lo largo del margen chileno entre los $19^o\, y\, 44^oS$.

2. Reproducir el campo de velocidades superficial intersísmica del antearco chileno evidenciado por datos geodésicos desde observaciones mediante GPS.

3. Determinar el rol de la geometría asociada a la megafalla de subducción a escala de tiempo del ciclo sísmico.

## 1.3. Marco tectónico y geológico del margen Chileno.

El margen Chileno es un tipo de zona de subducción , donde la placa de Nazca se desliza bajo la placa Sudamericana entrando en el manto subyacente (e.g., Jarrard, 1986; Turcotte & Schubert, 2002). La subducción es el principal responsable en la formación de cadena montañosa y volcánica en la placa continental de Sudamerica. La subducción de la placa de Nazca comienza a los $46^oS$ en la unión triple con la placa Antártica y Sudamericana, terminado por el norte $\sim 4^oN$ adyacente con placa de Cocos. La mayoría de las estimaciones de la tasa de convergencia contemporánea entre la placa de Nazca y Sudamericana se basan en el modelo cinemático global NUVEL-1A (Charles *et al.* , 1994) con una tasa de $77mm/año$. En base al cálculo del vector de Euler Nazca-Sudamerica se predicen una tasa de $68mm/año$ y mediciones geodéticas con una tasa actual de $66mm/año$ (Norabuena *et al.* , 1998; Angermann *et al.* , 1999).

La zona comprendida entre los $19^o$ y $44^oS$ de acuerdo a variaciones longitudinales en términos de topografía, tectónica y entre otras características esta zona se divide en : Andes centrales $(15 - 33,5°S)$ y Andes del sur $(33,5 - 47°S)$. Desde el punto de vista tectónico, la losa oceánica juega un rol en la segmentación del margen continental (Jordan et al., 1983; Gutscher *et al.* , 2000) La geometría de la placa subductada mantiene un angulo de subducción entre $20 - 35^o$ salvo entre los $28 - 35^o$ con una subducción horizontal, teniendo un rol importante en el control de primer orden en varios procesos de la placa superior, incluyendo magmatismo, acortamiento y el estilo estructural de la deformación de la corteza. Además, la topografía en relación con el espesor de la cortical el cual va disminuyendo de norte sur, alcanzando máximo espesor en el sector occidental de los Andes centrales $(65 - 70km)$. En este segmento se desarrolla una topografía de $4{,}000m$ (altitud promedio) que contiene el mayor plateau continental del planeta después del Tibet (Altiplano-Puna) y la mayor elevación del hemisferio sur (Monte Aconcagua). En cambio en el segmento Andes del Sur, el espesor cortical es inferior a los $40km$.

En la zona de los Andes del Sur, existen dos segmentos sísmicos bien delimitados, un segmento norte correspondiente a la zona de ruptura del terremoto Mw8.8 del Maule 2010 y un segmento sur que corresponde a la zona de ruptura del terremoto de Valvidia de 1960 asociado con la Zona de Falla Liquiñe-Ofqui (ZFLO) rasgo tectónico dominante de este segmento (Cembrano *et al.* , 2000). Su presencia limita el antearco hacia el Este. La Zona de Falla Liquiñe-Ofqui, es zona de cizalle dúctil y de movimiento dextral con rumbo $N10^oE$ (Arancibia *et al.* , 1999; Cembrano *et al.* , 2000) causado por la convergencia oblicua entre Nazca y Sudamérica.

## 1.4. Datos y Métodos

### 1.4.1. Vectores de velocidad superficial desde GNSS

Desplazamientos superficiales pueden ser obtenidos mediante la moderna geodesia satelital, en particular, el conocido Sistema de Posicionamiento Global (GPS) proporciona posiciones relativas sobre la superficie terrestre y con ayuda de herramientas de software (por ejemplo Bernese, Gamit/Globk, gLab, etc) se implementan estrategias de post procesamiento de los datos observados para determinar posiciones absolutas de los puntos de medición. Densos arreglos de estaciones se encuentran distribuidas a lo largo y ancho del margen chileno las cuales han proporcionado numerosas mediciones, pudiendo determinar desplazamientos de la superficie con una precisión de milímetros. La alta precisión que proporcionan las mediciones de GPS, permite estudiar la cinemática y la dinámica de los procesos de deformación actuales a lo largo de los límite de placas, permitiendo una mejor comprensión de los mecanismos de acoplamiento entre placas (e.g., Smith, D. & Turcotte1993; Scholz, 2002; Avouac, 2015) y de las fases del ciclo de deformación sísmica causadas por acople heterogéneo de la zona interplaca (Moreno *et al.* , 2008; Moreno *et al.* , 2012). La ubicación de los sitios o estaciones de GPS están vinculadas a diversos proyectos de investigación realizados por

diferentes universidades y centros de investigación extranjeras, en colaboración con universidades nacionales. La Fig1.4.1 muestra la distribuciones de alrededor de 500 estaciones y sus velocidades anuales publicados dentro de las últimas dos décadas al presente.

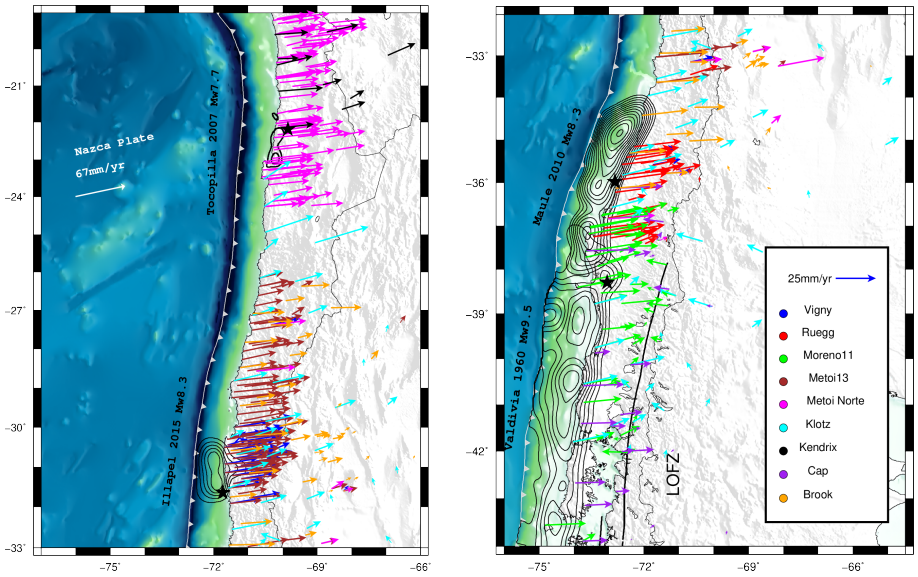


Figura 1.4.1: Distribución de estaciones de GPS y velocidades anuales del margen colisional Andino entre los 19º y 44ºS. Proyecto de los Andes Centrales (CAP) en el período 1994-2007 (Bevis *et al.* , 2000), South American Geodynamic Activities (SAGA) (Klotz *et al.* , 2001), observaciones previas al terremoto Maule Mw8.8 del 2010 (Moreno *et al.* , 2010; Ruegg *et al.* , 2009)

### 1.4.2. Método de Elementos Finitos

Definir o caracterizar el sistema de placas Andino es fundamental para entender su evolución y establecer la relación que existe entre los procesos superficiales de la corteza y los mas profundos al interior de la Tierra. Por lo tanto, es necesario conocer la distribución espacial de las propiedades físicas o relogía de las rocas. La reología gobierna su comportamiento en términos de deformación debido a las fuerzas a las que son sometidas en el interior de la Tierra. Por su parte, la corteza superior se puede considerar como un sólido elástico de Hooke $\sigma = \epsilon E$, es decir, puede ser modelada

por una relación elástica lineal entre el esfuerzo $\sigma$ y la deformación $\epsilon$. Sin embargo, al aumentar en profundidad, existe un aumento de presión y temperatura, lo cual provoca que el comportamiento de la roca a escala de tiempo de corto plazo, sea tanto elástico como viscoso, pudiendo ser descrito por una combinación lineal de un elemento elástico y viscoso de Maxwell.

Variados son los modelos elásticos y geométricos simplificados de subducción propuestos por varios autores (e.g. Zhao & Takemoto, 2000; Conrad *et al.* , 2004; Kanda & Simons, 2010), implementan modelos reológicos de elásticidad lineal con geometrías cercanas a la realidad con el fin de construir un modelo conceptual que pudiera describir el proceso de subducción y la deformación elástica asociada a la fase intersímica, Esto se logra mediante la implementación del Método de Elementos Finitos (F.E.M.), que es un método numérico versátil y poderoso, que permite aproximar soluciones de ecuaciones diferenciales parciales que describen diversos fenómenos físicos cuasi-estáticos y/o dinámicos mediante su discretización en tiempo y espacio. Una de las ventajas del FEM es la capacidad de manejar modelos geométricos complejos e implementar complejas condiciones de contorno y contactos entre superficies.

El comportamiento de la litósfera modelado por medio de una reología elástica, implica que la deformación $\epsilon$ que sufre la roca es proporcional al esfuerzo aplicado $\sigma$ y esta deformación desaparece al cesar el esfuerzo aplicado, recuperando la roca su forma original (notar que la deformación elástica de las rocas es limitada ya que las deformaciones son mínimas).

$$\sigma_{ij} = \lambda \epsilon_{ii} I + 2\mu \epsilon_{ij} \tag{1.4.1}$$

El comportamiento de un medio elástico de densidad $\rho$ sometido a una fuerza $f$ por unidad de volumen y un esfuerzo $\sigma$, queda determinado la ecuación elastodinámica, la cual relaciona las variaciones espaciales de los esfuerzos con los cambios temporales del vector desplazamiento $u$.

$$\sigma_{ij,j} + f_i = \rho \ddot{u}_i \tag{1.4.2}$$

Nuestro problema general es resolver a deformación permanente resolviendo para los desplazamientos $u$ en un medio elástico a la escala de tiempo del ciclo sísmico, por lo que las variaciones de tiempo relacionadas a la propagación de ondas sísmicas no son consideradas y por lo tanto $\ddot{u}$ es ignorado. Luego el problema se reduce a resolver la ecuación (1.4.3) (forma fuerte):

$$\sigma_{ij,j} + f_i = 0 \text{ in } V, \tag{1.4.3}$$

$$\sigma_{ij} n_j = T_i \text{ on } S_T, \tag{1.4.4}$$

$$u_i = u_i^o \text{ on } S_u, \tag{1.4.5}$$

La solución de la ecuación 1.4.3 puede ser obtenida en forma númerica aplicando el método de Galerkin, el detalle de solución se presenta en el Apéndice, Anexo I.

### 1.4.3. Geometría tridimensional de los Andes Centrales y Sur ($19^oS$ a $44^oS$)

Investigar cual es relación que pueda existir entre las diferentes variables un sistema tan complejo como lo es la zona de subducción, requiere de una etapa de desarrollo relevante y que consiste básicamente en discretizar el medio continuo de las principales estructuras que componen la zona en estudio,. La discretización de los dominios asociados a las diferentes estructuras que componen ambas placas exige el control de los elementos durante la generación de la malla de elementos finitos. Estos consisten de celdas linealmente equivalentes y en ellos se deben considerar algunos criterios: tipos de elementos, formas de elementos, control de densidad de lo elementos de la malla y eficiencia de tiempo (Ho-Le, 1988). El rendimiento del método de elementos

finitos depende fuertemente de la calidad de la malla final, por lo que se requiere previamente una etapa de remallado y refinamiento de acuerdo a los criterios anteriores, puesto que la malla final depende fuertemente de la calidad de la malla inicial.

La construcción de la geometría 2D y 3D se realiza interpolando perfiles de Oeste a Este a distintas latitudes, moviéndose de Norte a Sur, sobre datos de topografía y batimetría local digital SRTM con una resolución a 90m Fig1.4.2. Las estructuras internas de ambas placas se derivan del modelo de densidad 3D geofísicamente constreñido por Tassara & Echaurren (2012) proporcionando una malla con 5 dominios: el Slab con espesor uniforme de $30km$, la placa continental incluyendo la discontinuidad de Mohorovich y el límite litosférico, por último los respectivos mantos oceánicos y continental hasta una profundidad de 300km. La discretización de los límites que definen la placa oceánica, placa continental y el manto se realiza mediante una serie de perfiles Oeste-Este a distintas latitudes moviéndose de Norte a Sur (figura 1b). Con esta serie de perfiles se dispone de una serie de nodos de paso uniforme, generando un mallado tetrahédrico al interior del volumen y su posterior refinamiento mediante herramientas de software especializadas en mallado automático. Entre los muchos malladores existentes, en este trabajo de investigación se utilizaron los malladores Triangle y CUBIT. Triangle es un generador de malla de calidad bidimensional y un Triangulator Delaunay de libre distribución Por su parte CUBIT, es un conjunto de herramientas de software comercial con variadas funciones para la generación y descomposición de mallas en dos o tres dimensiones.

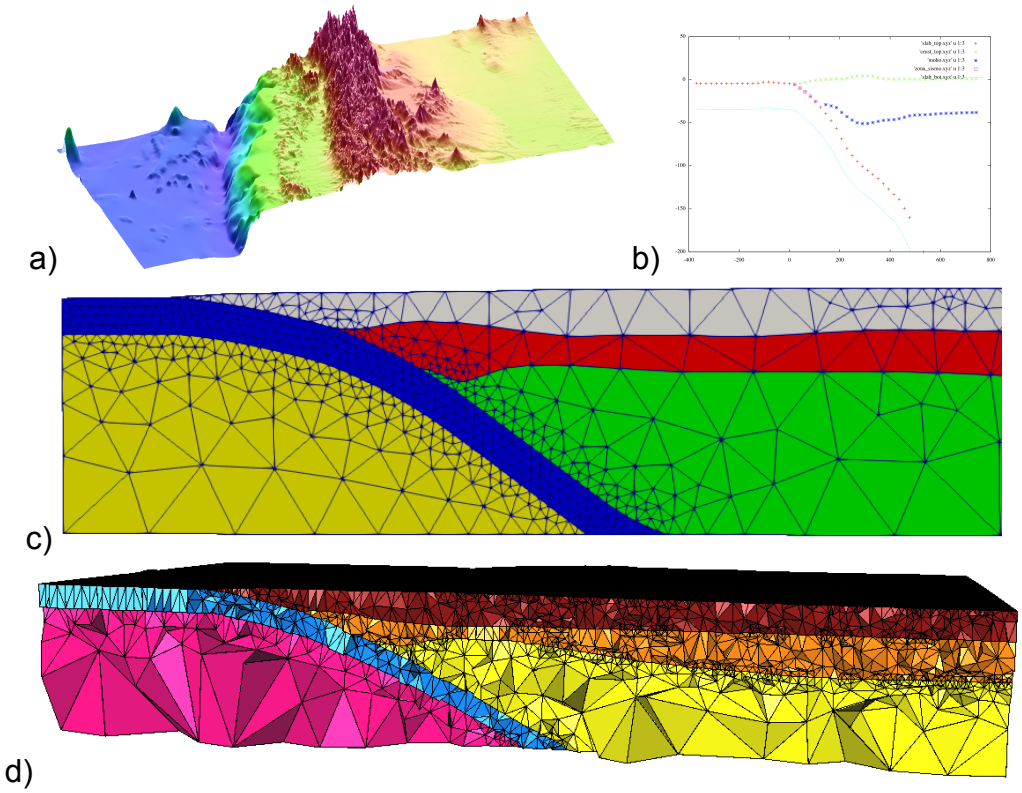


Figura 1.4.2: (a) Topografía desde una base de elevación digital SRTM entre los $33^o$ y $38^oS$, amplificda en un factor x10. (b) perfiles EW interpolados con GMT (Generic Mapping Tools) desde la base topográfica SRTM a los $35,5^oS$. (c) Geometría y mallado 2D no regular con elementos triangulares (d) Malla 3D no regular con elementos tetrahédricos. Las figuras (c) y (d) contienen la geometría 2D y 3D en ellos se distinguen cinco dominios reológicos: la placa oceánica, placa continental, manto oceánico y continental,

## 1.5. Estructura de la Tesis

Tras las interrogantes planteadas en la introducción, se pretende responder alguna de estas preguntas implementando modelos numéricos del sistema de subducción chileno mediante el método de elementos finitos y sus predicciones compararlas con datos de GPS intersísmicos a lo largo del margen chileno entre los $19 - 44^oS$. Previamente en el subcapítulo 1.4 se abordan los conceptos básicos de la modelación con

Elementos Finitos y mallado de la geometría del margen precisa utilizando datos geofísicos externos. En el Capítulo 2, se presenta un estudio bidimensional cinemático de placa elástica en subducción (ESPM) que explora la deformación elástica intersísmica a través de observaciones previas en el límite sur de la zona de ruptura del terremoto del Maule 2010. La deformación superficial fué modelada con la zona de contacto interplaca completamente acoplada y haciendo del variaciones en el límite inferior de acople así como variaciones de los parámetros elásticos de placas. Los resultados proporcionados son comparados con las predicciones hechas mediante el modelo de dislocación elástica BSM. Se observa que el modelo propuesto ESPM vincula los procesos de flexión de la placa elástica con la deformación intersísmica mediante variaciones de la tasa de deslizamiento reducidas en la base placa en subducción y manto subyacente, ayudando a aclarar bajo qué condiciones el BSM es apropiado para ajustar los datos geodésicos intersísmicos en los márgenes convergentes. El capítulo 3 es una extensión tridimensional del modelo 2D presentado en el caítulo 2, que pretende responder como contribuye la losa en flexión a la deformación cortical intersísmica, cuya geometría de margen se obtuvo de un modelo de densidad externo y el que se extiende lo largo del margen chileno manteniendo toda la zona de contacto simogénica completamente acoplada. Los resultados de la deformación intersísmica modelada muestran que la deformación del antearco esta acotada por la tasa de deslizamiento basal en la zona de flexura. Por último, en el capítulo 4 y 5, se presentan la discusión y las principales conclusiones de este trabajo de investigación.

## Capítulo 2

# Interseismic deformation at subduction zones investigated by 2D numerical modeling: case study before the 2010 Maule earthquake.

Contreras, M., Tassara, A., Gerbault, M., Araya, R., and Bataille, K., 2016, Interseismic deformation at subduction zones investigated by 2D numerical modeling: case study before the 2010 Maule earthquake: Andean Geology, v. 43, no. 3, p. 247-262., doi:http://dx.doi.org/10.5027/andgeoV43n3-a01

**ABSTRACT.** We study interseismic deformation preceding the Mw8.8 2010 Maule earthquake by means of two-dimensional finite-element modeling. Our goal is to gain insight into the fundamental factors controlling elastic strain build-up and release in subduction zones, and to evaluate different modeling approaches of surface displacement as observed by GPS. We developed a linear elasticity solver that allows us to implement a realistic subducting plate geometry constrained by geophysical data. We test the influence of subducting plate thickness, variations in the updip and downdip limit of a 100% locked interplate zone, elastic parameters, and velocity reduction at the base of the subducted slab. We compared our modeled predictions with interseismic GPS observations along an EW profile crossing the Maule earthquake rupture area, in order to

determine best fitting parameters. Our results indicate little influence of the subducting plate thickness at a given downdip limit, which itself has a strong influence on surface deformation. However, the fit to observations is achieved only after reducing the velocity at the base of the subducted slab below the trench region to 10% of the far-field convergence rate. We link this novel result to complementary numerical models that gradually evolve toward considering longer time-scales and complex rheology in order to evaluate the mechanical meaning of the above mentioned inferred kinematic conditions. This allowed us to link the velocity reduction at the base of subducting slabs with a long-term state of high flexural stress resulting from the mechanical interaction of the slab with the underlying mantle. Even a small amount of theses high deviatoric stresses may transfer towards the upper portion of the slab as strain energy that could participate into the mechanical loading of the megathrust and therefore in triggering large earthquakes there.

*Keywords:* *Interseismic deformation, GPS surface velocity, Maule earthquake, Stress, Subduction, FEM.*

## 2.1. Introduction

The megathrust interplate shear zone along subduction zones is seen to behave frictionally locked during the time lapse between two large earthquakes. Interplate locking during this interseismic period can be modeled by an elastic deformation of the upper plate that translates into the displacement of the surface in the direction of convergence, a mechanism that has been widely used to explain observations of conventional geodetic measurements (see for example Thatcher and Rundle (1984) and Hashimoto and Jackson (1993) who modeled century-long geodetic data in Japan). Modern satellite geodesy, mostly the Global Positioning System (GPS), has improved the measurement of surface displacement at centimeter-level accuracy, allowing a better understanding

of the mechanisms of interplate coupling and the generation of great destructive earthquakes and tsunamis (e.g. Smith and Turcotte, 1993; Scholz, 2002; Avouac, 2015). In order to connect geodetic observables at the Earth's surface and plate coupling along the megathrust fault at depth, different approximations can be used. In this contribution we use 2D numerical models of subduction zones to analyze the inf luence of different parameters and several plate boundary approximations (including the Back Slip Model, BSM and, Elastic Subducting Plate Model, ESPM) on kinematic and mechanical conditions accompanying the seismic cycle. To do his we constrain the deformation caused by different models using interseismic surface velocity vectors measured by GPS previous to the Mw8.8 Maule 2010 earthquake along a trench-normal transect located near the Arauco Peninsula in south-central Chile (Fig. 1).

The Back Slip Model (BSM, Savage, 1983) assumes that the megathrust is a finite fault embedded into an elastic media and simulates the interseismic period by a downwards slip of the upper plate's base along this fault, simulating the coupling of the forearc wedge with the descending oceanic slab. The kinematic downdip movement of this fault produces an elastic deformation that translates into a surface displacement, which compared with geodetic observations allows to constrain the backslip velocity and therefore the degree of fault locking. Although the BSM approach is an oversimplification of the geometrical and rheological configuration of a subduction zone, which cannot be used to gain understanding on the mechanical interaction between plates leading to earthquakes, its simplicity has allowed successful applications to geodetic data analysis and seismic hazard assessment in a number of subduction zones worldwide (e.g. Prawirodirdjo *et al.* , 1997; Mazzotti *et al.* , 2000; Khazaradze and Klotz, 2003; Chlieh *et al.* , 2008; Moreno *et al.* , 2010).

In the attempt to construct a conceptual model that could describe the subduction process in a more realistic way, and yet preserve the simplicity of the kinematic link between geodetic observations and plate locking, Kanda and Simons (2010) proposed

the Elastic Subducting Plate Model (ESPM). This model is based on a previous conceptualization of Zhao and Takemoto (2000) and considers a subducting elastic slab of finite thickness coupled to an elastic upper plate along the seismogenic megathrust zone that moves with respect to the surrounding asthenospheric mantle. The ESPM also includes the kinematic effect of slab flexure near the trench axis by considering a decreasing velocity gradient along the slab's radius of curvature. Plate flexure and its associated bending stresses have been shown to be a fundamental process that connects the dynamic force balance of tectonic plates with the seismic cycle (Conrad *et al.* , 2004; Capitanio and Morra, 2012; Schellart, 2009; Buffet and Rowley, 2006). As demonstrated by Kanda and Simons (2010), the ESPM mimics the deformation field caused by the BSM when the thickness of the subducting plate tends to zero . However, if at least a portion of these stresses is not continuously released in the shallow portion of the subduction zone, then the predicted surface velocities of both models can differ significantly. This conclusion implies that the interpretation of geodetic observations within the framework of more (ESPM) or less (BSM) realistic approaches for assessing the degree of interseismic plate locking (and the maturity of a seismic cycle), remains to be developed together with an understanding of its mechanical implications.

With the main aim of analyzing the mechanical implications of the ESPM on the kinematics and mechanics of plate subduction and its influence on megathrust seismogenesis, we present here a series of 2D numerical models that range from simple kinematically-constrained elastic rheology at short time scales (a year) to complex elasto-visco-plastic rheology at large time-scales (millions of years). First we present our own version of an ESPM as implemented using the finite element method (FEM), with validation against analytical solutions of elastic dislocation . Our method further allows to account for realistic geometries of a subduction zone and the introduction of gradients in the velocity distribution at the base of the subducted plate. In section 3, we apply our modelling method to GPS-derived surface velocities obtained years to months before the Mw8.8 2010 Maule earthquake (Moreno *et al.* , 2010; Ruegg *et al.* , 2009)

along a nearby trench-orthogonal transect near $37°S$ in south-central Chile (Fig. 2.1.1). At this latitude, the proximity of the coastline to the trench (ca. 100 km) allows appreciating surface deformation by land-based GPS stations. The exercise shows that in order to fit the geodetic observations, the velocity of the subducting slab at the base of the plate near the trench axis must be significantly reduced with respect to the far-field plate velocity. In section 4, we use other numerical modeling approaches (ADELI, Hassani *et al.* , 1997 and Paravoz Gerbault *et al.* , 2009) to investigate the meanings of this result in terms of the mechanical interaction between the subducting slab and the underlying astenospheric mantle. We compare the instantaneous stress field generated by kinematic and geometric configurations, similar to those applied to our initial elastic model, with larger time-scale subduction models. Such long-term models show that when bending builds up naturally as a consequence of continuous subduction of a competent plate, the high deviatoric stresses that accumulate at the bent base of the slab are located in a position equivalent to the region where a reduction of slab velocity was required in the EPSM to fit the geodetic data. We finally discuss the implications of these results in terms of the relationship between the state of stress in the long-term in a subduction zone, and short-term seismogenic energy release.

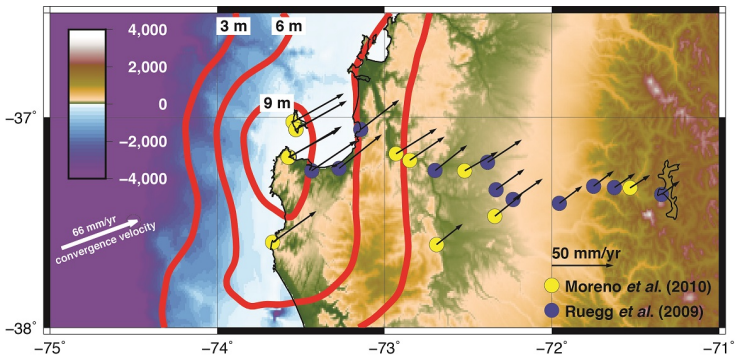


Figure 2.1.1: GPS-derived surface velocity vectors across a trench-perpendicular transect at 37.3ºS in south-central Chile (topography/bathymetry of the area is in gray tones). Vectors where calculated by Ruegg et al. (2009, blue dots) and Moreno et al. (2010, green dots) from measurements done before the Mw8.8 2010 Maule earthquake. Contours of 3, 6 and 9 m of co-seismic slip are shown in red (Moreno *et al.* , 2012) . The convergence velocity vector is shown as a red arrow

## 2.2. Finite element modeling of an elastic subduction zone during the interseismic phase

In order to simulate the elastic deformation produced by interseismic plate locking at subduction zones we use the finite-element method (FEM) to develop a 2D model in which displacement along a fault plane is implemented based on a split node technique (Melosh & Raefsky (1981)). We start with a conceptual model of an idealized subduction zone whose general configuration setup is shown in figure 2.2.1. This setup can indistinctly reproduce the BSM or the ESPM.For both models the subduction geometry is characterized by two parameters: $\Theta$ is the dip angle of the slab below the locked seismogenic zone and DDL is the depth to the Downdip Limit at which both plates are locked. For sake of simplicity as a first step, the DDL also corresponds to the limit between the upper plate and the underlying asthenospheric mantle (Fig. 2.2.1). Different domains (upper plate, subducting plate, asthenospheric mantle) can be recognized with eventually different values of the Young Modulus. The upper surface of the model is assumed to be stress free (i.e., it freely deforms) whereas along the lateral and bottom boundaries (extending down to 300 km in the mantle) no displacement is allowed (anchored boundaries). For the ESPM setup, a subducting plate of thickness H is defined and its motion is imposed as a boundary condition at its left-hand border. On the opposite edge of the slab at 300 km depth, free motion is allowed. In order to simulate the kinematic conditions of the interseismic phase, we impose a uniform slip along the boundaries of the elastic plate with the asthenospheric mantle (red lines in figure 2.2.1), and assume a 100%-coupled seismogenic zone (continuous deformation and stress in between the upper and lower plate from the top surface to the DDL depth). In contrast, in the simpler geometric setup corresponding to the BSM, a homogeneous slip is imposed along the seismogenic zone (blue line in figure 2.2.1) and all other boundaries are fixed.

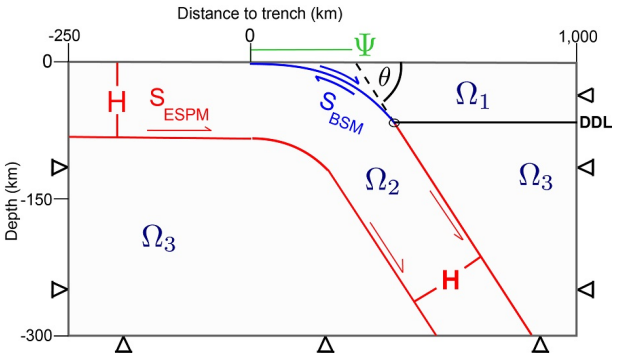


Figure 2.2.1: Model setup for the FEM experiments of subduction models. The figure define dimensions of the modeled space, boundary conditions, geometric parameters and different material domains ($\Omega_{1-3}$). For the ESPM configuration a slip $S_{ESPM}$ is imposed along the red slab boundaries and the interplate boundary (blue) is kept 100% locked, whereas for the BSM a backslip $S_{BSM}$ is imposed along the interplate boundary. See text for details.

## 2.3. Testing subduction models and FEM validation

### 2.3.1. BSM, an end-member case of ESPM

In order to first validate our model setup and to reproduce the analysis of Kanda and Simons (2010) with our finite element tool, we assign values of $40^{\circ}$ and 40 km for $\theta$ and DDL respectively, and crate two different models as shown in figure2.3.1; ESPM (Fig. 2.3.1a) and BSM (Fig. 2.3.1b). For ESPM we assigned 1 m of slip at the moving boundaries of the slab (red lines in figure 2.2.1) whereas for the BSM the same displacement is applied along the plate interface. In the limit when the slab thickness (H) of a ESPM tends to zero, the resulting deformation field should approach the one generated by a BSM, since the imposed displacements cancel each other except below the locked seismogenic zone, where slip at the base of the slab subsists and mimics backslip as for a BSM (Kanda and Simons (2010)). The displacement field resulting from the ESPM with a plate of thickness (H) of 5 km (approaching the case of a zero-thickness BSM) is shown in figure 3c and can be compared with the field generated by

the BSM in figure 3d. We see that both models generate an almost identical deformation within the volume of the upper plate: the norm of the displacement field decreases from a maxima at the trench to about 50% at location x=50 km, and to about 25% at location x=80 km.

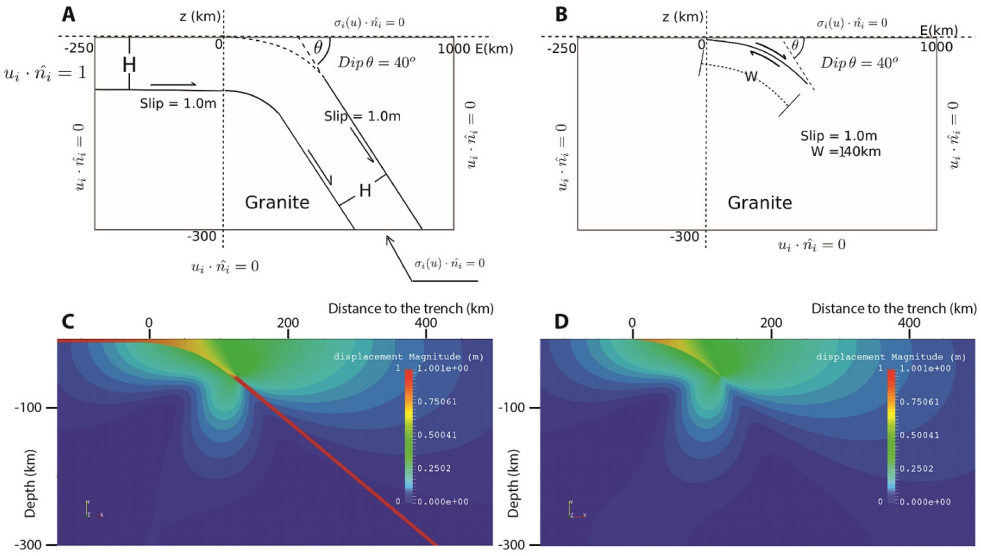


Figure 2.3.1: Comparison of BSM and ESPM with thickness H=5 km. Panels A and B show the model setup for a ESPM and BSM respectively. Lower panels depicts the calculated displacement field after applying 1 m slip to the boundaries of the slab in a ESPM (C) and the interplate boundary for a BSM (D)

The similarity between both models can also be appreciated in figure 2.3.2, which displays horizontal and vertical components of the surface displacement obtained from a BSM and from a ESPM with different plate thicknesses H between 5 and 50 km. Landward from the trench the solutions of the BSM and the 5 km thick slab ESPM are almost identical, while they both differ significantly with increasing slab thickness.

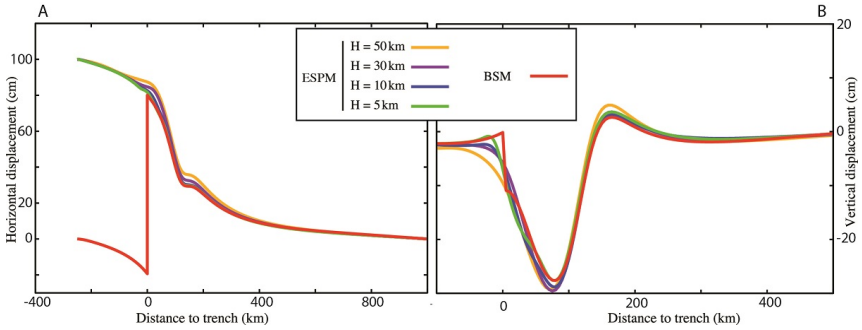


Figure 2.3.2: Comparison of horizontal (A) and vertical (B) surface displacement for BSM and ESPM with changing slab thickness H between 5 and 50 km.

Thus, the end-member ESPM with a nearly zero slab thickness can be efficiently modeled by a simple BSM, as shown by Kanda and Simons (2010) with their analytical formulation. This exercise serves as an independent validation of our numerical model.

### 2.3.2. Modeling interseismic deformation by BSM across the Arauco Peninsula before the 2010 Maule earthquake.

With the intention of offering an independent validation of our FEM approach, now we reproduce the BSM model proposed by Ruegg *et al.* (2009)to fit the GPS interseismic velocities measured before the Mw8.8 Maule 2010 earthquake. For this we use velocity vectors reported by Ruegg *et al.* (2009) and Moreno *et al.* , 2010 that were acquired during the decade preceding the Maule earthquake. These measurements are roughly aligned in a profile across the center of the Arauco Peninsula from the coastline extending east to the Andean volcanic arc near the Chile-Argentina boundary (Fig. 1). Ruegg *et al.* (2009) defined their BSM with a planar fault geometry characterized by the following parameters: Strike=0°, rake=−90°, DIP=17°, Up-Dip Limit UDL=0 km and width of the fault W=180 km. We constructed a 2D finite element mesh with these geometric parameters and imposed a backslip velocity of 65.5 mm/yr equal to the trench-normal convergence velocity.

Figure 2.3.3 compares the surface displacement predicted by the BSM analytical solution, which assumes the classical formulation of Okada (1985), with that computed with our ESPM FEM approach. It can be observed that both solutions are almost identical, mostly for the horizontal component, and that they fit the GPS data equally well.

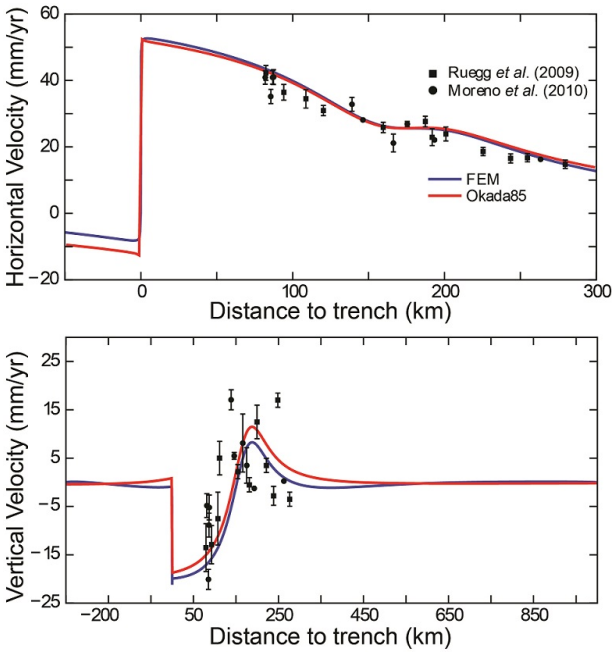


Figure 2.3.3: Modeled horizontal (A) and vertical (B) velocity and GPS observations (points with error bars) with the analytical solution of Okada (1985) and our FEM solution reproducing the same BSM parameters used by Ruegg et al. (2009).

## 2.4. Exploring parameters of the ESPM for interseismic deformation before the 2010 Maule earthquake

As recognized by Kanda and Simons (2010) and many others, a BSM approximation with a planar fault is an incorrect physical model of the process of plate subduction, and therefore we attempted to model the interseismic GPS data across the Arauco Peninsula with our ESPM approach. We first constructed a finite element mesh that interpolates

representative points of the local topography and bathymetry, as well as a realistic geometry of the slab upper surface (derived from the geophysically-constrained 3D model of Tassara & Echaurren, 2012). The upper plate has a constant thickness of 40 km.

With this FEM mesh (Fig. 2.4.1), we first study the influence of the slab plate thickness (which we assume constant across the model), the downdip limit (DDL) of the seismogenic zone, and variations of the elastic parameters between different domains. We assume the same boundary conditions as those defined for the conceptual ESPM (section 2) and apply a displacement of the oceanic plate from the left-hand side equal to 65 mm/yr, simulating its trench-normal motion during one year. The locked zone between the Nazca and South American plates is considered fully locked in-between the trench and its downdip limit (DDL), which can vary between 26 and 60 km depth in our simulations. Additionally, we considered variations of the elastic parameters of each domain $\Omega$ (see figure 2.2.1) in order to quantify their effect on surface displacements. Following the values given by Turcotte and Schubert (2002) we consider these domains to be dominantly composed by granite, granodiorite and/or peridotite with a Young modulus $E\,0.5,\ 1.0$ and/or $1.5x10^{11}Pa$, respectively.

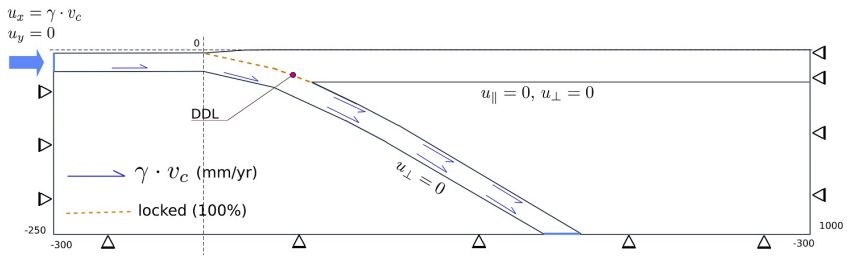


Figure 2.4.1: Model setup for a ESPM across the Arauco Peninsula near. The slab geometry was constructed according to the 3D geophysical model of Tassara and Echaurren (2012). The figure shows applied boundary conditions and defines main parameters of the model (see text for details).

With this setting, we try to reproduce the interseismic horizontal surface displacement observed with the GPS data. In a first attempt, we express a potential reduction of velocity at the bottom of the slab ($v_{bcs}$) with respect to the applied convergence velocity ($v_c$), which results from plate bending at the trench (Kanda and Simons, 2010). This

velocity can be evaluated geometrically and it is non-uniform below the seismogenic zone as defined by $v_{bcs} = \gamma((1 - H/R)/(1 - H/2R))$, with H the thickness of the slab and R its local radius of curvature. $\gamma$ is a parameter between 0 and 1 that allows us to express this reduced velocity at the base of the slab.

Figure 2.4.2a (horizontal component) and 2.4.2b (vertical component) show that, for a granodioritic upper plate with peridotitic slab and mantle, with $\gamma = 1$ and at a given DDL, varying the slab thickness H between 10 and 50 km has little effect on horizontal surface displacements, which appear significantly smaller than the uncertainty in GPS measurements. Variations in DDL in turn have a much larger effect. A DDL at 27 km depth produces deformation concentrated towards the trench, whereas a DDL near 60 km depth shifts the surface deformation towards the volcanic arc with an excess of deformation in the forearc near the coast. The best-fitting combination of DDL and H under the described conditions is accomplished for values of 42 km and 30 km respectively (Fig. 2.4.2a and b), although we note that none of the models is really able to give an acceptable fit to the GPS data. This difficulty in reproducing the observed interseismic surface displacements with an ESPM approach remains independent from the choice of elastic parameters for each model domain.

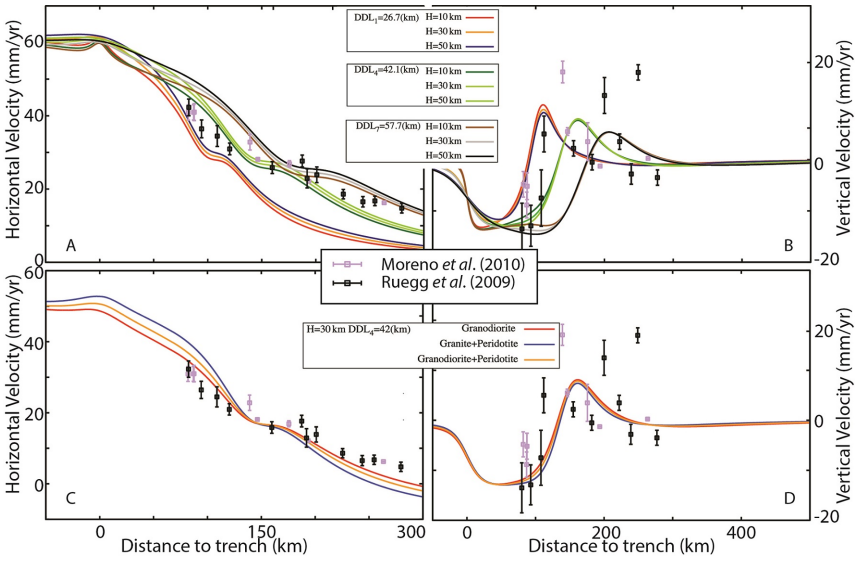


Figure 2.4.2: ESPM Model results compared with GPS velocities along the Arauco Peninsula. Left-hand and right-hand panels show horizontal and vertical velocities respectively. With respect to uncertainties of GPS observations, surface displacement produced by the ESPM with realistic subduction geometry is almost insensitive to slab thickness H (as shown in A and B). Young Modulus E of the upper plate has a minor effect (as shown in C and D). Displacement is mostly controlled by the Downdip Limit (DDL) of interplate locking. Even our best fitting model (H=30 km, Granodiorite, DDL=42 km) is unable to reproduce the observed GPS velocities.

We then show that this misfit can be corrected by introducing a reduction in the velocity at the bottom of the subducting plate below the coupling zone. Now we consider the same configuration as described in the previous section, but we modify the velocity distribution along the bottom boundary of the subducting plate, as illustrated with arrows of different colors in figure 2.4.3. One configuration considers that this basal velocity is constantly reduced by a factor $\gamma$=0.1 with respect to. When we apply this velocity reduction to the entire curved bottom of the slab, the resulting surface deformation is largely reduced well below the level given by GPS measurements (black curve in figure 2.4.4). However, if we apply this reduced velocity along the bottom of the slab from the trench only down to the DDL depth, then the match to GPS observations is strongly improved (blue curve in figure 2.4.4).

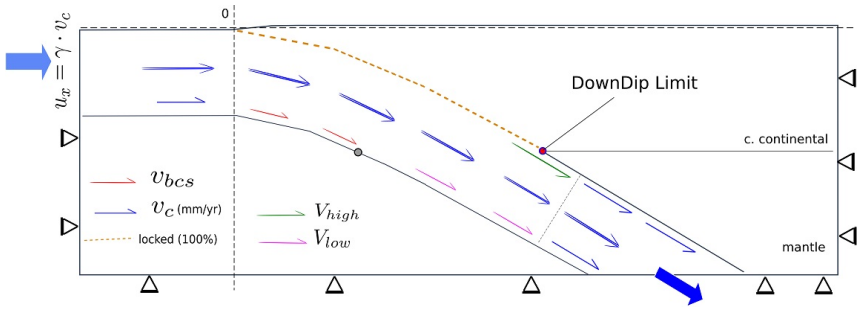


Figure 2.4.3: Model setup for an ESPM with reduced velocity at the base of the slab due to bending. This is similar to figure 2.4.2 but here we introduce the possibility of reducing the displacement velocity at the base of the slab compared with the rest of plate as shown by arrows of different colors.

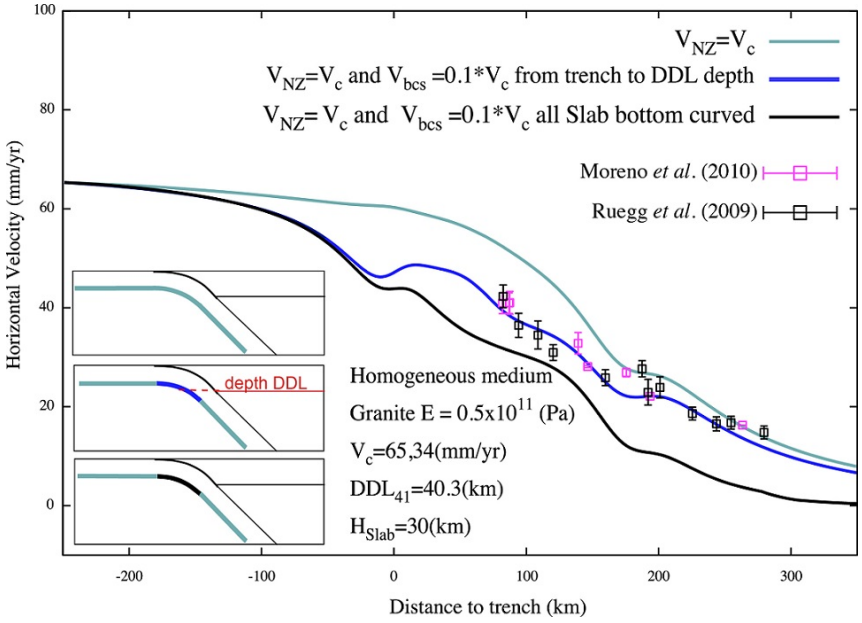


Figure 2.4.4: Horizontal surface velocity resulting from a ESPM model that incorporates velocity reduction at the base of the slab. Our best ESPM notably improves the fitting to observed GPS rates if the velocity at the base of the slab is strongly reduced to 10% of the convergence velocity.

## 2.5. Mechanical interaction between subducted slab and mantle

In searching for a dynamic explanation to the necessity of a localized velocity reduction at the base of the subducted slab, we explore now with complementary numerical models the mechanical interaction between a subducting plate and its underlying mantle. Beginning with boundary conditions similar to those imposed in the previous section, e.g., thought to be appropriate for slab-mantle interaction at the short-scale, we progressively evolve towards boundary conditions appropriate for long-term slab-mantle interaction. We thus discuss step by step the implications of some assumptions, and how our reasoning brings insight on interseismic seismogenic behavior.

### 2.5.1. Stress field resulting from kinematic conditions imposed at the slab-mantle interface

To explore how the kinematic conditions applied in the previous ESPM models of sections 3 and 4 actually translate into mechanical interactions between the slab and the underlying asthenospheric mantle, we first use the FEM-based code ADELI (Hassani *et al.* , 1997; Cattin *et al.* , 1997; Provost & Chery, 2006), which has already been used to study various mechanical aspects of the seismic cycle as well as long-term subduction, and presents the advantage of handling pre-defined contact zones enabling relative motion between different space domains. In the models below we consider synthetic geometries, since the aim here is to identify the theoretical influence of kinematic conditions along the slab-mantle interface on the stress field.

We define a first numerical setup (Adeli Model AM-O, Figure 2.5.1a) in which the underlying mantle is considered as an inviscid fluid. Therefore it does not need to be included in the physical mantle domain (as in e.g., Hassani *et al.* , 1997). . This setup

considers identical kinematic conditions along the plates to those assumed in the previous sections, with applied tangential velocity at the base of the subducting plate, and a fixed base of the overriding plate. The interaction with the overriding plate is simulated as a locked contact zone of high friction, simulating interseismic coupling (e.g., Cattin *et al.* , 1997). The gravity force is included (to the difference of ESPM models of previous section).. Assumed to behave as an inviscid fluid. Note that the deviatoric shear stresses that develops inside both plates are of the order of 100 and 200 MPa (turquoise to green, identical in all three cases. Figure 10a displays the resulting internal stress field inside the slab (of the order of 100 MPa), resulting from the imposed velocity discontinuities at the base of the two plates. Two zones of discontinuous stresses develop in the upper plate in the forearc area (magnitude of about 200 MPa)

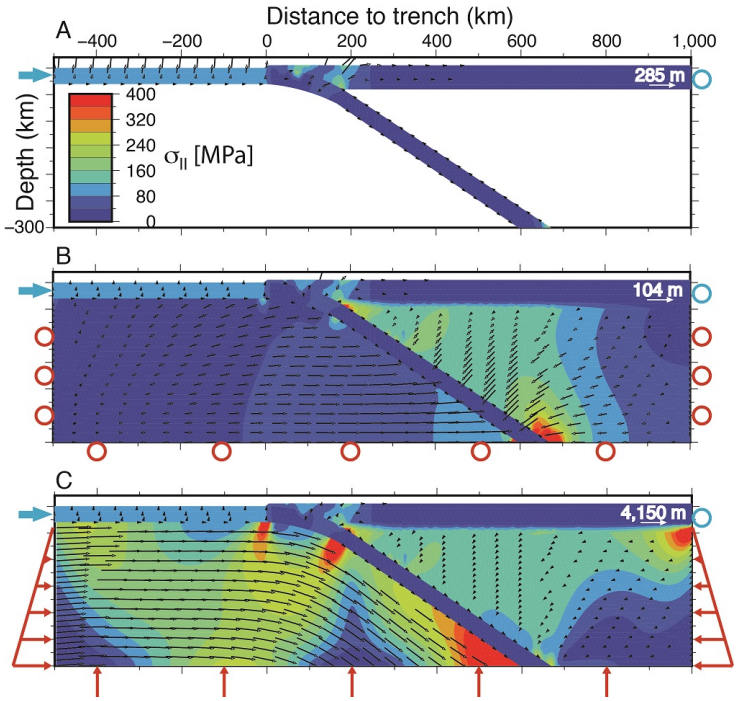


Figure 2.5.1: Three models set with code ADELI, in order to illustrate the mechanical interaction between the slab and the mantle, Each three cases impose a tangential velocity along the base of the subducting plate, and no motion at the base of the overriding plate (as in the previous section). The deviatoric shear stresses that develop inside both plates reach ~100-200 MPa (turquoise to green), and are identical in all three cases. However, all 3 cases assume different conditions for the underlying mantle. A. Model AM-0 assumes that the mantle behaves as an inviscid fluid; B. AM-1 includes a mantle with temperature dependent viscosity (on average, of the order of $10^2$ Pa.s): its lateral and bottom borders are set free-slip (similar to models in section 3). C. AM-2 includes a mantle of similar rheology but its boundaries react to Archimedes' restoring force (as if embedded in an infinite half space). The large stress field generated in the mantle results from the kinematic conditions applied on to the base of the plates, thus showing that they are out of mechanical balance.

If now we incorporate the mantle in our models, a conceptual issue appears: when one accounts for the flexed geometry of a slab inside the mantle, one must also think of the mechanical effects of this flexure. This mechanical effect is usually thought of as tension on the top of the bent slab and compression in its inner corner. However, the mantle underneath is also loaded, and deformed in association to this slab bending.

Considering a plate that subducts from rigth down to the left, the surrounding mantle thus receives a clockwise torque from above, and flows accordingly to balance this torque (for maintenance of the mechanical equilibrium of the entire medium). Even though the mantle domain is visco-elastic and likely dissipates high stresses via low viscosity flow, mechanical balance must still be assessed. Consequently, how do the kinematical conditions imposed on the base of a subducting plate as defined in sections 3 and 4, fall within this frame-view of slab-mantle mechanical interaction?

When incorporating the mantle in numerical models of subduction, one must define the boundary conditions acting on its boundaries, either with kinematic or stress conditions. We test both options in the subsequent two models AM-1 and AM-2 (Fig. 2.5.1b and c). First, in AM-1 we prescribe free-slip boundary conditions on the lateral borders and bottom base of the mantle (as in models of previous sections). Upon applying a displacement of 1 meter of the subducting plate in this model (during 100 yrs), the resulting state of stress inside both subducting and overriding lithospheres is very similar to AM-0. However, to the difference of AM-0, now large deviatoric stresses also appear in the mantle underlying the overriding plate (much greater than 200 MPa, Fig 2.5.1b).

In the second model AM-2 (Fig. 2.5.1c), Archimede's lithostatic stress reaction force is applied along the boundaries of the modeled mantle domain (e.g., simulating that the modeled domain is embedded in an infinite half space, as in e.g., Gerbault *et al.* , 2009or Burov et al., 2005). The resulting state of stress displays even larger deviatoric stresses both in the eastern and western parts of the modeled mantle. This stress field results from the kinematic constraints that we imposed onto the base of the slab and the overriding plate, and which exert a flexural torque on the mantle. The resulting stress fields in both models AM-1 and AM-2 show that the flexure of natural subduction zones are actually not balanced in a simple way (e.g., not only geometrical) with the imposition of kinematic conditions on the slab-mantle interface. In other words, the application of the specific kinematic conditions proper to the ESPM produces large stresses in the underlying mantle. We show here with these three models (AM-0,1,2) that mechanical

equilibrium is a significant issue, that is not resolved along the plate interface alone, and despite the fact that the stress distribution inside the slab remain similar in all three cases.

Let us now show another model AM-3 (Fig. 2.5.2a), in which we allow the slab to slide freely above the underlying mantle (thus no imposed velocity and no resisting friction). Now gravity is turned off again, and only boundary velocities are applied at the far-field right-end and at the bottom intersection of the slab with the modeled domain. A typical flexural pattern develops within 100 yr with bending stresses of the order of 200 MPa inside the slab (Fig. 2.5.2a). In the surrounding mantle in turn, no high stresses develop, in contrast to models AM-0,1,2. One cannot avoid recognizing the existence of slab bending stresses within the frame of plate tectonics at the long-term scale of millions years. So now we are faced with the problem of deciding if the boundary conditions at the slab-mantle interface associated to slab bending at the long-term, also correctly simulate the same slab-mantle interface at the scale of the seismic cycle. In the quest for assessing the appropriate kinematic conditions that control interseismic deformation, one may (or may not) assume that slab bending is negligible when considering relative shear motion (from one earthquake to the other). In order to further clarify the importance of long term deformation and stress pattern, we present in the next section a last model that simulates the long-term flexural behavior of a subducting plate.

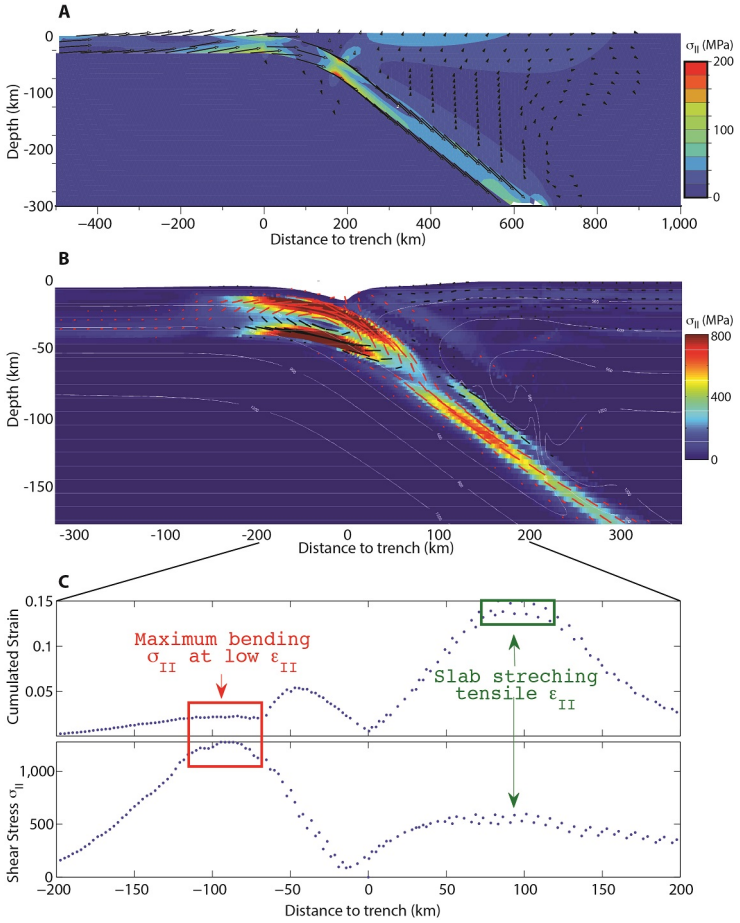


Figure 2.5.2: Stress distribution inside an elastic plate when considering long-term subduction. A. Model AM-3, produced with code Adeli, with no gravity field, and with freely sliding plate-mantle boundaries (along which neither tangential nor normal motion are imposed). Within ~300 kyr of applied convergence from the right-hand side of the model (as in AM-2), flexural deviatoric stresses up to 260 MPa (in red) develop inside the elastic plate; B. Model LM built with code “Parovoz” (modified from Gerbault et al., 2009). Here gravity is included and the mantle and overriding plate both behave according to thermally dependent elasto-visco-plastic laws. Therefore their boundary is self-consistently defined and evolves throughout the time duration of the model. Within 4 Myr of applied far-field convergence, flexural stresses of the order of 1,000 MPa develop inside the elastic portion of the slab. Black and red lines display the orientation of principal tensile and compressional stress, respectively, typical of a flexural pattern; C. Profiles along the base of the slab in LM, determined by the isotherms around 600 ºC: depth of profile (upper profile), accumulated shear strain (middle), and shear stress (second invariant, bottom). At the slab’s corner around X=-50 km stresses exceed 1,000 MPa, whereas the shear strain remains low (red rectangle domain). Such a stress concentration is equivalent to a frictional resistance that explains the need to reduce artificially the eastward velocity in this bend in the FEM-based kinematic ESPM.

### 2.5.2. Long-term flexural stresses

Here we illustrate how flexural stresses develop in the long-term in a subduction zone. Therefore we display model LM, which is built with the finite-differences code Parovoz (Poliakov & Podladchikov, 1992), and assumes conditions similar to those defined by Gerbault *et al.* (2009), Dorbath *et al.* (2008) and Sobolev & Babeyko (2005) when studying the influence of rheology on deformation along the Chilean margin over several millions years. This model considers subduction over a time-scale of 4 Myrs and assumes self-consistently defined temperature-dependent elasto-visco-plasic rheology. Therefore the slab-mantle boundary is also self-consistently defined and consists in a continuous transition from competent (effectively elastic) plates to low viscosity asthenosphere. The setup is defined with the synthetic geometries of a bent slab which is pushed from its right-end side, eastward at the velocity of 4 cm/yr, while the overriding plate is remained fixed (free-slip far-field left-end of the model). At the base of the model domain the slab is also pulled downwards in the direction parallel to its inclination, at 4 cm/yr. As a result, flexural stresses build up and equilibrate within 4 Myr (Fig. 2.5.2b), using the flexure of the resistant slab to equilibrate the applied boundary conditions. Figure 2.4.2b displays the stress field via its 2nd invariant. Highest values occur where slab curvature changes: these stresses approach 1 GPa at the bottom corner of the flexed lithosphere (sampling of the displayed values was made at depths corresponding to the 590-620 ºC isotherm interval, Fig. 2.5.2c). Thus we illustrate here that although the bent corner of the slab does not undergo much internal deformation (red rectangle domain in figure 2.5.2c), it actually stores large bending stresses capable of exceeding the brittle-yield strength.

Two side comments rise from these models. First, the large stresses that develop in this model result from our assumption of purely visco-elastic behaviour in this case, in order to remain consistent with the other models of the present study. If rheologies were assumed fully elasto-visco-plastic as in e.g., Gerbault *et al.* (2009), then the stresses would remain bounded by the yield strength and would not exceed ~400 MPa. However

the strain and stress field still both develop a similar pattern to that displayed here. Second, if we compare more precisely the location of these large bending stresses with respect to the position of the trench, one notes that in model LM (Fig. 2.5.2b) they are offset by about 50 km further to the left of the trench and are generally more inclined with respect to the horizontal, in comparison with the AM models. This difference is due to the different designed initial geometries (plate length and curvature between Adeli and Parovoz), but does not affect the mechanical implications of our study.

In comparing the AM0,1,2 models with the AM3 and LM models we see that the imposition of specific velocities along the base of the slab, despite accounting for its realistic motion, actually impedes the development of flexural stresses inside the slab. That is the reason why high stresses develop in the mantle in models AM0,1,2 (Fig. 2.5.1), that counter balance the imposed velocities. In contrast in the long-term model LM, although the base of the bent slab is inherently kinematically locked with the low-viscosity underlying mantle, large stresses rather develop inside the slab itself since it is the solicited competent body under flexure.

Slab bending is actually involved in the energy balance that makes the dynamics of a subduction zone (Buffett, 2006;Ribe, 2010; Capitanio & Morra (2012); Fourel *et al.* , 2014. Bending stresses are intricated with the other driving and resisting forces and the energy balance does not provide similar quantities depending on the assumptions of the different authors. For instance downwards in the asthenosphere, bending energy is involved in the low viscosity asthenospheric flow that accompanies subduction a the scale of the entire upper mantle (e.g., viscous drag, Hager and O'Connell, 1978; Piromallo *et al.* , 2006 ; Li *et al.* , 2014 ). Downwards along the axis and inside the slab, bending is at least partly restored by slab unbending, as seen in figure 11b with a reversed orientation of the tensile/compressional stresses at ~100 km depth (e.g., Buffett, 2006; Hassani *et al.* , 1997; Čížková *et al.* (2007) ; Faccenda & Mancktelow, 2010 ). Upwards above the slab, this energy must also, very likely, be partly released in some manner.

Since pressure decreases, large stresses are no longer sustained (brittle failure occurs). However deformation is eased, and we can imagine that “stress” is transformed into “deformation”. Let us thus propose a simple back of the envelop exercise. Let us assume energy conservation between the bottom and top of a lithospheric column set right in the bent corner of the slab: if the shear stresses are about 10 times greater in the deep domains with respect to the top domains at the slab’s bend (100 to 400 MPa as opposed to 10 to 40 MPa along the seismogenic zone, e.g., Lamb, 2006; Tassara, 2010), then energy conservation (expressed as the product of stress and strain rate) implies that the deformation that is to be released at the top of the slab should be 10 times greater than that along the base of the slab. Coincidentally, in order to fit the surface (top) interseismic deformation in the ESPM model of section 4, we had to reduce the velocity applied along the base of the slab by a similar factor of 10 (in the bent corner). This reasoning is consistent with the concept that stored (shear) stress at the bent base of the slab transfers towards its upper portion into (shear) strain. Unfortunately, deciphering the amplitude of this energy transfer with respect to other processes requires assessing non-linear temporally and spatially scaled parameters (such as speed of stress and strain guides in the deforming pores of the bent lithosphere, with respect to the above mentioned other modes of energy transfer), which falls out of the ambitions of the present paper.

## 2.6. Conclusions

The well known Back Slip Model (BSM; Savage, 1983) solution of an elastic dislocation in a semi-infinite half space (Okada, 1985), is widely used to predict interseismic deformation along a given fault zone and has been efficiently applied to model GPS observations before the 2010 Maule earthquake (Ruegg *et al.* , 2009; Moreno *et al.* , 2010). However, the BSM can not give insights into the physical and mechanical processes properly taking place at subduction zones because it exclude the presence of

the subducting plate. Consequently we have developed a two-dimensional finite element approach simulating interseismic elastic deformation at subduction zones, which accounts for realistic interplate geometries and allows to apply kinematical constraints along the base of the subducting lithosphere. Similarly to Kanda & Simons (2010), our Elastic Plate Subducting Model (EPSM) confirms that the BSM solution is identical to the solution of an EPSM when plate thickness is negligible. Our EPSM geometrical setup was then constrained by independent geophysical data, and fitted with the observed GPS surface rates across the Arauco Peninsula. A satisfactory fit was obtained only when we reduced the basal velocity at the corner of the slab below the trench to 10% of the total convergence rate after correction of the geometrical effect of slab bending.

This velocity reduction likely represents the kinematic consequence of stress dissipation caused by plate bending near the trench axis, as suggested by complementary mechanical models that explore the slab-mantle mechanical interaction. These complementary models reveal that purely kinematic conditions applied to the slab impede the build-up of flexural stresses inside the slab and thus generate out of balance stresses in the adjacent mantle. The inherent flexural stresses associated with a naturally bending slab are shown to concentrate indeed at the basal corner of the subducting plate. Such high bending stresses thus explain the artificial reduction in basal velocity that we had to apply to our EPSM in order to fit GPS interseismic observations, and allows us to state that the slab-mantle boundary acts as an efficient frictional interface in the bent corner of the slab. This statement is consistent with the argumentation of Buffett (2006) that bending of the subducting plate exerts a basal friction that opposes to the motion of the downgoing plate, and that the driving forces of subduction include slab flexure (Forsyth & Uyeda, 1975), which is partially balanced by local resistance Conrad *et al.* , 2004.

Our study shows that in order to retrieve appropriately the mechanical processes in play during interseismic deformation, numerical models should account for the effects of plate flexure, thus pointing to the perspective of integrating both short-term and long-term approaches (e.g., Van Dinther *et al.* , 2013). Meanwhile, the careful application of

locally reduced basal velocities in an ESPM approach offers a more realistic treatment of GPS interseismic surface displacements than the conventional BSM approach.

## 2.7. Acknowledgements

We thank fruitful discussions with R. Hassani and M. Moreno. This research was funded by Fondecyt Projects 1101034, 1151175, ECOS/Conicyt C13U03, DFG/Conicyt PCCI130039, DAAD/Conicyt 2058-2010. The detailed review of F. Aron allows us to greatly improve the clarity and quality of this contribution.

## Capítulo 3

# Mechanical modeling for interseismic deformation at subduction zones: Influences of slab curvature in interseismic deformation along the Chilean margin

*M. Contreras*[*1,2], *A. Tassara*[3] *and M. Moreno*[4]

[1]*Programa de Doctorado en Ciencias Geológicas, Facultad de Ciencias Químicas, Universidad de Concepción, Concepción, Chile.*

[2]*Facultad de Medicina, Universidad San Sebastián, General Cruz 1257, Concepción Chile.*

[3]*Departamento de Ciencias de la Tierra, Facultad de Ciencias Químicas, Universidad de Concepción, Concepción, Chile.*

[4]*Departamento de Geofísica, Universidad de Concepción, Concepción, Chile.*

*Corresponding author, Email mcontrerask@udec.cl

***This article it was submitted to Geophysical Research Letters.***

**ABSTRACT.** Improving the representation of interseismic deformation at subduction zones is crucial for determining the locking degree at the megathrust, its slip deficit and seismic potential. We implement a new approach considering the far-field motion of a 3D finite-thickness subducting slab and its bending underneath the trench. For

simplicity we assume that both plates are fully locked along its frictional contact, which is defined between the trench and the intersection of the continental Moho with the slab top surface. We apply our approach to the Chilean margin and note that surface velocities predicted by our simple forward model fit GPS observations in a first order. Regions where residuals are larger than GPS uncertainties can be readily related to specific processes that are not included in the model, as the translation of rigid blocks, postseismic deformation of the 1960 Valdivia earthquake or a possible preseismic signal before the 2010 Maule earthquake.

## 3.1. Introduction

The steady downward pull of the oceanic plate during the interseismic period induces a strain accumulation along the seismogenic part of the plate interface in response to its frictional behavior (e.g., Marone, 1998). The rate of the plate convergence accumulated as slip deficit is defined kinematically by the degree of locking, with a maximum locking degree of 1 indicating that the rate of slip deficit accumulation is equal to the rate of plate convergence (e.g., Klotz *et al.* , 2001; Chlieh *et al.* , 2008; Bürgmann *et al.* , 2005). Geodetic observations of recent large subduction-zone earthquakes have revealed a spatial correlation between the extent and magnitude of coseismic ruptures and the degree of locking along the plate interface (Chlieh *et al.* , 2008; Perfettini *et al.* , 2010; Moreno *et al.* , 2010; Loveless & Meade, 2010; Schurr *et al.* , 2014). Therefore, mapping and understanding the physical control of plate-interface locking have become a topic of prime interest, as it is relevant for understanding seismic hazard.

Estimates of locking distribution rely on the wealth of the geodetic data, modeling assumptions (geometry, structure, prescription of slip) and inversion technique (e.g., Du *et al.* , 1992). Due to different assumptions in the locking models, maps of locking distribution even for same areas that use similar data are very different (Moreno *et al.* , 2010, Métois *et al.* , 2012; Métois *et al.* , 2013; Chlieh *et al.* , 2011; Schurr

*et al.* , 2014). Hence, there is a need to thoroughly improve the scientific basis behind locking estimations and to better interpret the physical meaning of spatial variations of locking degree. Interseismic fore-arc deformation, which is mainly driven by locking of the subduction megathrust, also affects the whole margin volume, including plastic and viscoelastic deformations. Despite this complexity, interseismic deformation has been frequently simulated using the Back-Slip Model (BSM) (Savage, 1983) in an elastic half-space (Okada, 1985). The BSM considers that the strain accumulation during the interseismic period is the superposition of a steady state that represents the long-term average motion and a supplemental solution that compensates the steady-state term. By adding both contributions a no-slip condition is generated, which mimics a kinematic locked plate interface. However, the BSM assumes that all the interseismic deformation is attributed to the no-slip condition only at the top of the Slab and supposes that no permanent deformation accumulates on the long-term. Together with these questionable assumptions, the BSM basically represents the locking deformation as the slip of a normal fault at the plate convergence velocity along the locked zone, which does not correspond with the actual mechanism associated with the interseismic strain accumulation. A more physically based model is the Subducting Plate Model (SPM) (Kanda & Simons, 2010), which considers deformation in the subducting and overriding plates taking into account the elastic thickness of the slab, and also allowing rheological variations. This model includes steady aseismic slip at the bottom of the Slab and on the top of the Slab below the seismogenic zone. No slip conditions are introduced along the locked portion of the seismogenic zone. Thus the SPM integrates the geometry of the Slab (thickness and curvature) within the simulation of interseismic deformation, providing a model with more mechanical foundation with respect the BSM. Along the same line, we implement a new approach to improve the SPM that expand in 3D a previous 2D version of our model (Contreras et al., 2016) and considers the long term contribution and the bending term of the curvature of the slab across the seismogenic zone. We show in particular that our simple approach can simulate the interseismic deformation

recorded by GPS data in the entire Chilean subduction zone without any complexity on the locking distribution along the megathrust.

## 3.2. Methodology

We implement a 2D and 3D kinematic elastic model to reproduce surface displacements during the interseismic phase along of the Andean margin through the use of the software for modeling of elements finite PyLith-2.13 (Aagaard *et al.* , 2013), a Python open source tool that implement the finite element approach for the solution of lithospheric problems. Finite element meshes were constructed both for the case 2D across the Arauco Peninsula, as well as the 3D case along of the Southern Andes in-between $19^o$ to $44^oS$. Geometrically both models consist of four elastics domains (upper plate, subducting plate, continental and oceanic asthenospheric mantle), incorporating not only the geometry of the continental and subducting plate, but also topography and continental Moho. Both 2D and 3D model geometry were they derived from the geophysically-constrained 3D model of Tassara and Echaurren, 2012. To simulate the interseismic phase, our model considers the subducting plate of finite thinckness that is fully locked along the interplate boundary with the upper plate from trench to the intersection of the megathrust with the continental Moho discontinuity. In this particular case, for a seismogenic zone with high coupling degree, the surface displacements observed by GPS are due to the existence of non-homogenous slip rate at the base of the slab that dissipates the high flexural stress as resulting from the mechanical interaction of the slab with the underlying mantle in the long term (Contreras *et al.* , 2016). Therefore, depending on the distribution of the slip rate between the slab and underlying Asthenospheric mantle, we observe that the surface displacements from GPS are in between a maximum and minimum range displacement as result of two states of elastic deformation in function of the slip rate. We have defined the kinematics of the subducted plate during the interseismic phase, considering an elastic framework and pure bending. With the purpose of

delimiting the surface displacements as a function of a slip rate at the based of the Slab, we defined an elastic plate in subduction with an thickness ***h*** and fully locked seismogenic zone (called Elastic Subducting Plate Model $ESPM$), which produce a maximum deformation state. In the same way, the long-term contribution $ESPM^{(1)}$ produces as a minimum state of elastic deformation when we fix to fully locked both the seismogenic megathrust and the bottom boundary of the slab delimited by the points AB below de seismogenic zone as in (Fig.3.2.1). Both states are controlled imposing a sliding along the bottom limit of the Slab with the underlying mantle. Therefore, it is possible to take values of convergence velocity between $0$ and the convergence velocity $v_c$ (mm/yr), which implies that the plate in subducting slab is freely sliping above the asthenosphere and in others it is kept coupled to the mantle. Particularly in the area where the Slab is under bending, the slip rate takes on a value lower than that the velocity developed in the center of the plate under a frame of pure bending. However, in an $ESPM$ configuration, we impose a slip rate equal to $v_c$ for producing the maximum surface displacements in the upper plate to delimit the surface displacements. On the other way, the long-term contribution $ESPM^{(1)}$ produce the minimum surface displacements when we impose zero slip on the curved base of the Slab while the rest of the slab-mantle boundary is sliding simulating the convergence with uniform velocity and equal to $v_c$.

We start with a simple configuration setup in 2D across the Arauco Peninsula, that was based on an idealized elastic subducting plate model (ESPM), as proposed by Kanda & Simons (2010). To simulate the oceanic plate in subduction, we divided the slab into two kinematical domains. A first domain that we have called $ESPM^{(1)}$ in the previous section, it is defined in the slab limits with a convergence velocity $v_c$ equal to 6,534[cm/yr]. The second domain $ESPM^{(2)}$, is characterized by the zone where the plate is flexed for which the convergence velocity is varying respect to the radius of curvature. Its central plane maintains the convergence velocity with the same value defined in the domain $ESPM^{(1)}$, and at the bottom curvature of the slab, it develops the minimum velocity value respect to the center of the plate. Both domains $ESPM^{(1)}$

and $ESPM^{(2)}$ are illustrated in Fig.3.2.1 with blue and green respectively. Besides, we assume the seismogenic zone between the Nazca and South American plates is fully locked in-between the trench and the Moho discontinuity.

Respect to the rheological compositions, we consider three models in which oceanic, continental plate and asthenospheric mantle that are defined as purely elastic characterized by differents values of the Young Modulus. In this linear elastic framework, the displacement produced at the surface results from superposition or contribution of slips imposed at the limits of the slab in this two kinematical domains, that is to say, $ESPM = ESPM^{(1)} + ESPM^{(2)}$.

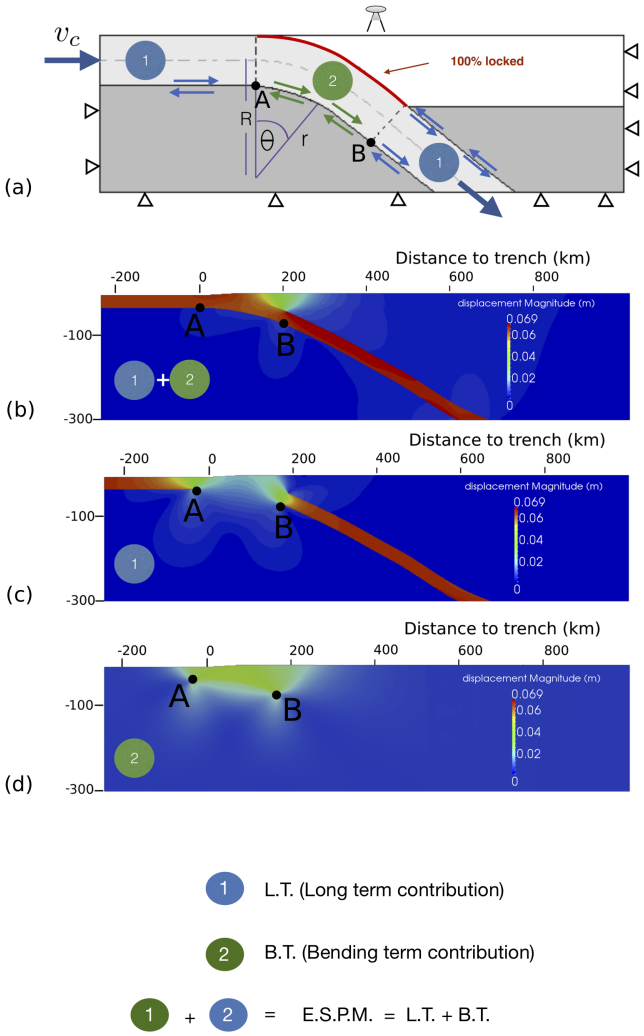


Figure 3.2.1: (a) Simply setting of a 2D subduction zone showing two kinematical domains. Blue circle labeled with number one, represents the long-term contribution $ESPM^{(1)}$ and the green circle labeledd with number two is the contribution along flexural zone $ESPM^{(2)}$ such $ESPM = ESPM^{(1)} + ESPM^{(2)}$. Red line is the seismogenic zone fully locked in-between the trench and the Moho discontinuity.

## 3.3. Modeling interseismic phase before the 2010 Maule earthquake

### 3.3.1. 2D interseismic model along Arauco Península.

We apply our modeling method to GPS-derived surface velocities along a nearby trench-orthogonal transect near $37°S$ in Arauco Península, south-central Chile. These velocity vectors were acquired during the decade preceding before the Mw8.8 2010 Maule earthquake, as reported by Moreno *et al.* (2010) and Ruegg *et al.* (2009). The displacement field arising from the $ESPM$ and $ESPM^{(1)}$ forward models are shown in Fig.3.2.1(b)-(c), and the respective horizontal and verticals displacements on the surface are showing in Fig.3.3.1. The blue curve it shows the surface displacements due to the slab subducting with constant displacement along the slab-mantle boundary and fully locked seismogenic zone. We observed that subtracting from the $ESPM$ only the displacements generated by $ESPM^{(1)}$, as shown in red in Fig.3.3.1, the difference between the surface displacement due to $ESPM$ and $ESPM^{(1)}$ does corresponds to the displacements observed by GPS.

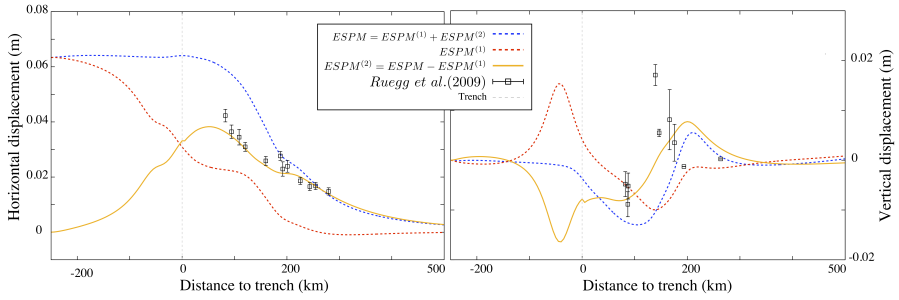


Figure 3.3.1: Horizontal (left) and vertical (right) surface displacement. The yellow line is the surface modeled displacement and fits the GPS displacements observed reported by Ruegg et al. (2009) before Maule earthquake 2010 ($GPS \approx ESPM - ESPM^{(1)}$).

### 3.3.2. 3D model for Interseismic phase along of the Southern Andes in-between $19^oS$ to $40^oS$

According to the results obtained in section 2, the difference $ESPM - ESPM^{(1)}$ it is a good approximation to the displacements observed by GPS in a seismogenic zone with high coupling degree. Therefore, we extend our methodology in 3D and apply it along of the Andean margin between $19^oS - 44^oS$, i.e. the region covered by the geophysically-constrained 3D model of Tassara & Echaurren (2012). To simulate the interseismic deformation associated with the oceanic crust subduction according to the simple configuration setup of ESPM in 2D illustrated in Fig3.2.1(a), we impose aseismic slip to the subducted slab along its boundary with the underlying asthenospheric mantle with oblique convergence at 67(mm/yr) oriented $78^oN$. The interface between the oceanic plate and continental forearc is fully locked in-between the trench and the Moho discontinuity. According to our definition of $ESPM^{(1)}$ it is necessary to delimit the slab arc AB (as in Fig.3.2.1), or the 3D case is to evaluate the effective deviatoric stress generated by the model in one year. Fig.3.3.2 shows a view of stresses developed at the bottom of the slab. The area where the plate is flexed is delimited with two lines segmented, labeled with A and B. This area considers high values of deviatoric stress per cell, from where approximately the slab begins to bend the point B, which was measured radially from the intersection of Moho with the Slab.

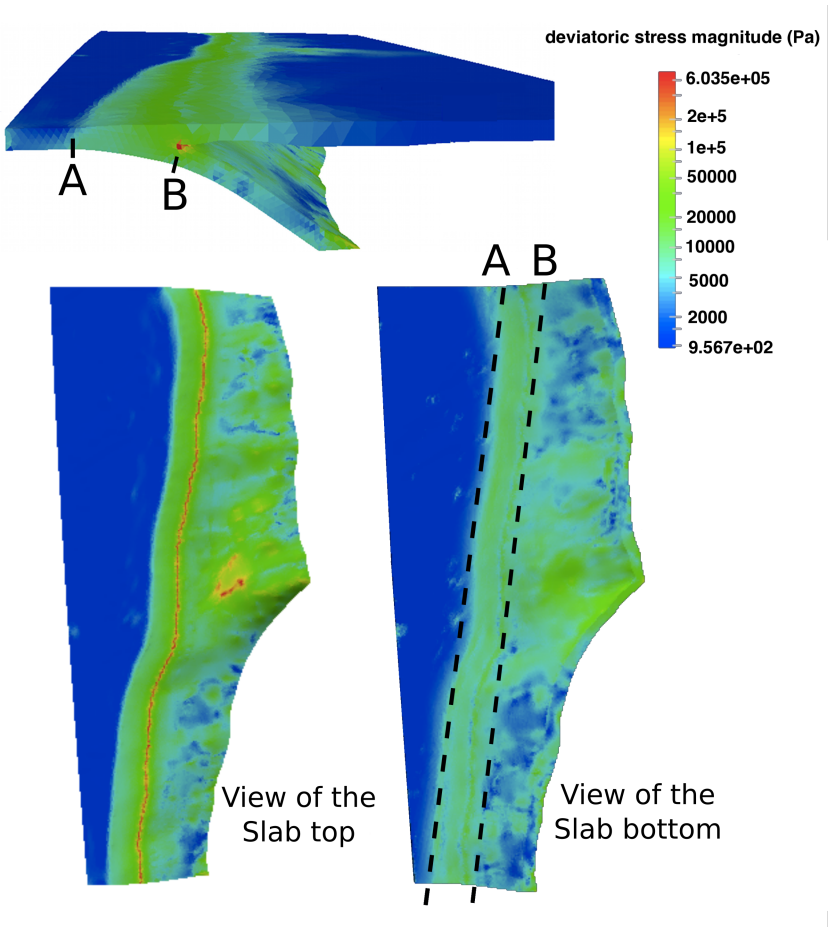


Figure 3.3.2: Deviatoric stress during a year produced in an elastic subducting plate model with uniform slip to 67 mm/yr at the interface Slab-mantle in oblique convergence and fully locked seismogenic zone in-between Trench and Moho discontinuity. The points A and B, delimit the zone where the Slab is bend, in our model they are below the seismogenic zone is fully locked ( in-between the trench and Moho discontinuity).

Once the limits of the bended slab are defined, we kinematically load the system with the convergence velocity for both extreme ESPM models and get the resulting surface deformation field that we evaluate at points coinciding with the available GPS velocity vectors in order to compare our predicted displacements aginst the observed velocities. Fig.3.3.3 shows predicted and observed velocity vectors and a map interpolated from the magnitude of the residual vector at each observation point. It also includes EW cross-sections comparing horizontal velocity computed with our model and GPS

observations at latitude $19^o$, $23^o$, $33^o$, $37^o$ and $41^oS$. When we compare the surface displacements predicted by the $ESPM - ESPM^{(1)}$ model against the observed GPS velocities (after correcting by the postseismic viscoelastic signals of the Valdivia earthquake 1960, Moreno *et al.* , 2012), we note a very good fit both in map view and in the EW cross-sections.

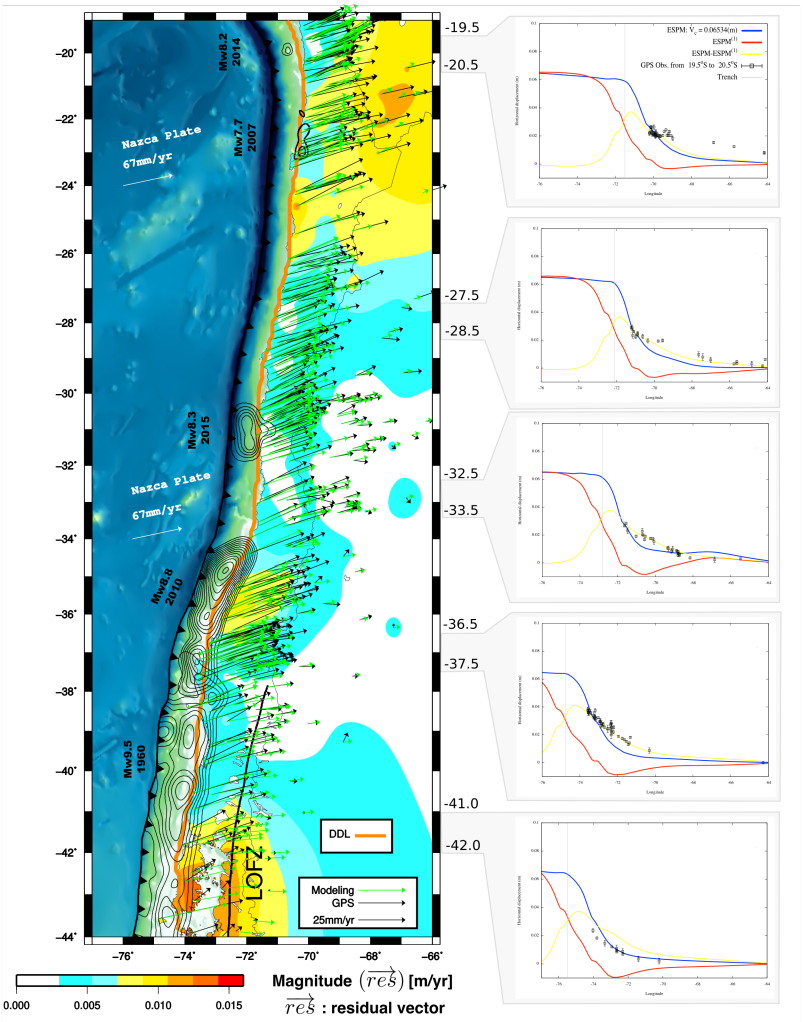


Figure 3.3.3: Surface displacements modeled $ESPM - ESPM^{(1)}$ versus compilation of GPS data before the 2010 Maule earthquake and corrected for postseismic viscoelastic signals of the Valdivia earthquake 1960. The modeled vectors and observed, are shown with green and black arrows, respectively. Left panel, is shown profiles EW to 19, 23, 33 and 37S, the yellow line is the curve modeled and fits the GPS observations dotted in black squares.

## 3.4. Discussion

GPS derived surface velocities before large earthquakes along the Andean margin have been previously modeled using the simple Back Slip Model BSM (i.e. Ruegg *et al.* , 2009; Chlieh *et al.* , 2004Chlieh et al., 2006; Moreno *et al.* , 2010; Métois *et al.* , 2012). The common BSM considers a uniform blocking of the megathrust during the interseismic period, between the trench and up to a depth of 40-50 km, explaining the first order deformation pattern. Most of the models that implement the BSM consider a simple interplate boundary without the presence of a subducting plate and therefore they cannot correctly predict the state of stress associated with the coupling of plates (Douglass & Buffeft, 1995). On the other hand, as stated by Kanda & Simons (2010), when we consider the thickness of subducting oceanic plate and its curvature, the effects of slab bending due to the imposition of kinematic conditions in the oceanic plate are included in a more natural way, which is more consistent with the conceptual model of subduction.

The kinematic conditions imposed in our model by sliding rates along the slab bottom surface clearly identify two kinematic domains, which when superimposed contribute to the deformation field that can be observed by GPS at the surface. This, it is possible to linearly separate the influence on surface deformation due to the far-field plate motion and slip below the bended slab near the trench. As shown in Fig. 4, predictions of our model explains much of the observed GPS velocities, with nearly 75% of the residuals with magnitudes lower than the average error of the GPS velocities (5 mm/yr). By construction of our model, this implies that motion of the slab at its base below the bended zone for a fully locked interplate boundary is the main mechanism responsible of the interseismic deformation field of the upper plate. Note that the location of the slipping zone at the base of the bended slab is defined by points A and B of Fig.**??** that resulted from large gradients in the deviatoric stress caused by the curvature of the slab under the kinematic load of plate convergence. Particular, the location of point B tends to coincide with the downdip limit (DDL) of the seismogenic zone, which is defined by

the intersection of the Moho with the slab that itself coincides with the position of the coastline at the surface.

Although the model efficiently represents the data in the first order, there are regions where the residuals are greater than the average error and require explanation as they reflect other processes not included in the basic conceptual model. In the zone of the Altiplano plateau ($19 - 24^oS$) high residuals are obtained in direction to the continent that could reflect the movement of a Altiplano block as a rigid entity, as also inferred by previous authors (Allmendinger *et al.* , 1997; Bevis *et al.* , 2001; Brooks *et al.* , 2011; Métois *et al.* , 2012 ) that indicate up to 10 mm/yr of shortening in the back-arc sub-andean fold thrust belt associated with the present day construction of the orogen. When observing the residuals vectors (supplementary material), they have a homogeneous magnitude and direction consistent with the rotational movement of a rigid block (i.e., the orogenic block of the plateau Altiplánico) towards the east.

Other region of relatively high residual magnitude is the area affected by the Mw9.5 Valdivia 1960 earthquake that coincides with the northward moving Chiloé forearc sliver (Wang, 2007) along the arc parallel Liquiñe Ofqui Fault Zone (LOFZ). Residual vectors with high magnitude pointing to the trench (supplementary material) indicate that the model generates an excess load with respect to the observations. This exceeding load can be caused by several reasons: 1) 1960 postseismic effect on the megathrust that inhibit the complete re-blocking of the fault and therefore induce a heterogeneous coupling that is less than 100% as used in our model Moreno *et al.* (2011) . 2) 1960 postseismic relaxation of the viscous mantle and lower crust inducing deformation of the forearc and arc in the direction of the trench that has not yet completely been relaxed and decreases the magnitude of the vectors in the direction of convergence (Hu *et al.* , 2004, Khazaradze, 2002). As our GPS observations to the south of $36^oS$ were corrected by a possible postseismic viscoelastic relaxation after the 1960 earthquake (as derived by Moreno *et al.* (2011) from a coseismic slip pattern and a generalized Maxwell solid rheology model), this interpretation seems less likely. 3) A possible DDL

shallower than the intersection of the Slab with continental Moho as assumed in our model, which seems reasonable if we consider the young age of the Nazca plate in the trench in this region (<20 Ma) that means. A warm subducting slab implies that the intersection of the continental Moho with the slab top lies likely deeper that the $350 - 400^oC$ isotherm that has been commonly considered the upper bound for the frictional behavior along the megathrust (Oleskevich *et al.* , 1999; Wang, 2007). 4) Interestingly, the residuals show a northward direction in the Chiloé area near the LOFZ. This suggests a northward translational movement of this block consisting of magnitude and direction with the inferences of Wang et al. (2007).

By the other hand, for the area affected by the Mw8.8 Maule 2010 earthquake, the model predicts interseismic surface velocities that are lower than those observed by GPS data years before the earthquake. Into the conceptual basis of our model, particularly considering that we impose a 100% locking between both plates, this under prediction may suggest that during the preseismic phase of the Maule earthquake the DDL was deeper than the intersection of the slab with the Moho as used here. This could be justified by the fact that coseismic models of this earthquake (i.e. Lay *et al.* , 2010; Tong *et al.* , 2010; Lorito *et al.* , 2011; Moreno *et al.* , 2012) generally show slip larger than 1 m until depths of 40-50 km, well below our DDL. An alternative explanation is that observed GPS velocity vectors in excess to model predictions are caused by a local and transient acceleration of the subduction velocity or an excess slab pull at depth, as has been also suggested by patterns of intermediate depth seismicity before large megathrust earthquakes for the Maule earthquake and elsewhere (i.e. Bouchon *et al.* , 2016; Jara *et al.* , 2017; Bloch *et al.* , 2018).

## 3.5. Conclusion

We have developed an alternative methodology for to the study the interseismic elastic deformation at subduction zones, which accounts for realistic interplate geometries applying kinematical constraints along the base of the subducting lithosphere. Our model geometrical setup it was constrained by independent geophysical data, and fitted with the observed GPS surface rates along de Southern Andes Chilean subduction margin between $19^oS$ and $44^oS$. The adjustment was obtained with low residues, mainly in GPS stations located near the coastline as a result of the difference between two states of deformation with a seismogenic zone completely blocked until the Moho discontinuity and slip at the bended base of the subducted slab ear the trench. The general good fit between model predictions and GPS observations demonstrates that the rates of interseismic surface displacement are mainly due to the effects of the slab flexion in subduction. As we impose a 100% locking between both plates along the seismogenic zone, spatial variations of GPS velocities are naturally explained by our model as caused by variations in the geometry of the interplate boundary and location of the flexed base of the slab that we define by means of a large deviatoric stress. Regions where our model generates an under or overprediction of surface velocities with respect to GPS observations can be related with processes that are not included in our conceptual formulation. This is the case of a rigid block rotation and translation of the Altiplano, northward trench-parallel block motion of the Chiloe sliver in southern Chile, unrelaxed viscous stresses loaded by the giant Valdivia 1960 earthquake, or preseismic signals. Particularly intriguing is the exceeding observed velocity of GPS stations located around the rupture zone of the great 2010 Maule earthquake, that into the conceptual framework of our model can be related either to a downdip extension of the fully locked seismogenic zone behind the intersection of the continental Moho with the slab top surface and/or a transient acceleration of subducting velocity of the slab with respect to the loading convergence velocity as likely caused by an increment of slab pull. The

mechanical simplicity of our model makes it easy to apply to other subduction zones around the world with good GPS coverage, a future exercise that could allow us to test our main results and expand the reach of our conclusions.

## Acknowledgement

The authors would like to acknowledge finacial support of FONDECYT project 1151175 and Millenium Nucleus NG160025 “The Seismic Cycle Along Subduction Zones”.

## Capítulo 4

# SÍNTESIS Y DISCUSIÓN

El proceso de suducción de tipo Andina, por definición implica la inmersión de placa oceánica por debajo de la placa continental hacia el manto superior asumiendo una tasa de convergencia uniforme, proceso conceptual ampliamente aceptado en la comunidad científica (e.g., Forsyth & Uyeda, 1975; Hager, 1984). Sin embargo, este proceso frecuentemente no se ve reflejado en simulaciones cinemáticas de la fase intesísmica, fase modelada básicamente mediante el Back Slip Model (BSM) (Savage, 1983) como el deslizamiento de una falla normal a la velocidad de convergencia de la placa a lo largo de la zona de bloqueo (e.g. Chlieh *et al.* , 2004; Ruegg *et al.* , 2009; Métois *et al.* , 2012). El BSM es una simplificación excesiva de la configuración geométrica y reológica de una zona de subducción, que no puede utilizarse para comprender la interacción mecánica entre las placas.

Desde el punto de vista cinemático, la geometría y las fuentes de deformación sobre la base de modelos conceptuales previos (Zhao & Takemoto, 2000; Kanda & Simons, 2010), el modelo implementado en este trabajo es consistentes con el modelo conceptual de la subducción. Al considerar el espesor de la placa oceánica subductora y su curvatura, los efectos de la flexión de la losa debido a la imposición de condiciones cinemáticas en la placa oceánica se logran incluir de una manera más natural, lo que es más consistente con el modelo conceptual de subducción. En el Capítulo 2, se demostró numéricamente mediante el método de elementos finitos F.E.M., que el modelo de dislocación elástica BSM (Savage, 1983) aplicado a la fase intersísmica forma parte del

Modelo de Placa Elástica Subducida (o ESPM) cuando el espesor de placa oceánica es despreciable o nulo. Sin embargo, aunque el BSM es capaz de reproducir el campo de deformación intersísmica del antearco (e.g. Ruegg *et al.* , 2009; Moreno *et al.* , 2010), este carece de sentido físico como fuente de deformación de la subducción. Ahora, si el ESPM implementado es más consistente con el modelo conceptual de subducción ¿Por qué no es capaz de reproducir la tasa de desplazamiento intersísmica superficial para estaciones de GPS cercanas a la fosa?. Considerar que la velocidad de convergencia en la placa oceánica sea uniforme (desde de mediciones geodéticas o cálculo del vector de Euler) no es del todo correcto. La placa en subducción cerca de la fosa es sometida a flexión y suponiendo que se encuentre idealmente bajo flexura pura la velocidad de convergencia varía radialmente. En particular, en la base doblada de la losa la tasa de deslizamiento es menor que la de convergencia. Entonces, la deformación cortical transmitida desde una zona sismogénica completamente bloqueada, es función de la curvatura basal de la placa subductada. Como se mostró en el capítulo 2, las restricciones cinemáticas impuestas en la zona basal de la placa oceánica bajo la fosa son resultado del bending, el cual ejerce fricción basal que se opone al movimiento descendente de la losa en subducción (Buffett, 2006), luego el deslizamiento depende de la interacción mecánica con el manto subyacente. Estas condiciones mecánicas permiten una buena simulación de las observaciones por GPS en el antearco, lo que implica que el ESPM representa una buena respuesta a la deformación elástica de la litósfera influenciada por el bending sobre la escala temporal del ciclo sísmico.

En el Capítulo 3, se extiende el análisis a tres dimensiones y a gran parte del margen de subducción Chileno, en este capítulo se intenta responder ¿qué tan importante es la contribución de la losa en flexión a la deformación cortical del antearco? y en consecuencia si la contribución de la largo plazo de la losa también contribuye de alguna forma en la deformación del antearco. El modelo ESPM asume como restricción que la zona de contacto sismogénica permanece completamente acoplada desde la fosa hasta la discontinuidad del Moho, esta restricción actúa como una cota superior

en términos del acople sismogénico y en consecuencia también de la deformación del antearco, producto de imponer un deslizamiento uniforme en los bordes de la placa en subducción y el mato subyacente. Ahora si a la deformación total, dada por la configuración ESPM, le restamos la contribución de largo plazo de subducción, el resultado es que la deformación intersísmica por acople sismogénico se debe solo a la zona que se encuentra en flexura, esta zona es la que reproduce en gran medida el patrón de desplazamientos observados por GPS cercanos a línea de costa a lo largo de margen Chileno en estudio. Los resultados del modelo se resumen en la Fig.3.3.3, estos dan cuenta de que el movimiento de la losa en su base por debajo de la zona de flexión es el principal mecanismo responsable del campo de deformación intersísmica en la placa superior. El modelo no logra reproducir del todo los desplazamientos observados a lo largo del margen Chileno, existiendo zonas con altos residuales, entre los $19^o - 44^oS$ los vectores residuales en magnitud y dirección sugieren la presencia de un bloque en la meseta del Altiplano, esta interpretación coincide con lo expuesto por otros autores que sugieren queel pliegue subandino activo y el cinturón de empuje argentino pueden acomodar parte de la convergencia, hasta 10 mm/año (Norabuena *et al.* , 1998; Bevis *et al.* , 2001). En el extremo Sur, en la zona de ruptura del terremoto de Valdivia Mw9.5 del 1960 también existen vectores altos residuales. Una de las razones es que el modelo no incluye la zona de falla Liquiñe-Ofqui, la cual posee un movimiento hacia el norte paralelo a la fosa (Arancibia *et al.* , 1999; Cembrano *et al.* , 2000). Otra razón del por qué existen vectores residuales de gran magnitud y que en particular en esta zona apuntan en dirección hacia la fosa, puede ser al efecto postsísmico del terremoto de 1960 que induce un reacoplamiento de la megafalla de subducción inferior al 100 % (Moreno *et al.* , 2011) Por otro lado el límite inferior de acople nuestro modelo pudo haber sido mas somero, por encima de la isoterma de 350°C, la cual se relaciona con la profundidad de acople interplaca en la faseintersísmico (Oleskevich *et al.* , 1999; Wang, 2007).

El enfoque del modelo ESPM en esta tesis es capaz simular el campo de desplazamiento intersísmico registrado por los datos GPS en la mayor parte de zona de subducción Chilena y sin ninguna complejidad en la distribución del bloqueo a lo largo del megathrust, El ESPM proporciona un punto de vista alternativo al Back Slip Model (BSM), pero con una base mecánica que soporta el modelo conceptual de subducción, caracterizándolo frente al BSM con dos parámetros adicionalas: el espesor de la placa y el estres flexural. Si bién aumenta el número de parámetros (el espesor y la curvatura) esto permitiría introducir tasas de deslizamiento en la base de la placa oceánica para inducir deslizamientos en el megatrusth controlados por alguna ley de fricción (Scholz, 1998) Esto tendría el potencial para determinar variaciones espaciales del grado de bloqueo sin la necesidad de utilizar alguna técnica de inversión (e.g. Du *et al.* , 1992)

## Capítulo 5

# CONCLUSIONES

Los resultados logrados en el desarrollo de esta investigación contribuyen a una mejor comprensión del proceso de subducción y de la deformación cortical intersísmica que se produce en de los Andes Centrales y del Sur de Chile. Modelos desde el punto de vista cinemático, restringido por observaciones geodésicas y geometrías de placas derivados de modelos de densidad constreñidos por datos geofísicos, simulan correctamente los procesos físicos y mecánicos que tienen lugar en las zonas de subducción y reproducen el campo de velocidades GPS.

Las principales conclusiones del modelo elástico de placa subductada aplicado al margen colisional Andino se resumen en :

1. Zonas con un alto grado de acople en la zona de contacto sismogénica, muestran que los desplazamientos modelados encajan bastante bien con las observaciónes geodésicas contemporaneas principalmente en estaciones ubicadas cerca de la linea de costa. Estos estan relacionados a las variaciones de los desplazamientos basales de la placa en subducción. Esto implica que la heterogeneidad del grado de acople estimada usando BSM de la zona sismogénica es en realidad consecuenciade la interacción dinámica entre el slab y manto subyacente.

2. El modelo de placa elástica en subducción, demuestra que la cinemática aplicada a bordes de placas en zonas de subducción geométricamente mas cercanos de la realidad son físicamente más consistentes para modelar el ciclo sísmico. Las restriciones cinemáticas impuestas en la zona basal de la placa oceánica curvada

son consecuencia de alta tensión por flexión, lo que confirma que la interfase entre el manto y la losa posee un comportamiento friccional que se opone al movimiento descendente de la losa en subducción.

3. Los resultados obtenidos considerando las condiciones cinemáticas y de acople mecánico en el modelo 3D de placa elástica en subducción, evidencian que la deformación intersísmica producida en el antearco se deben en su mayor parte a los desplazamientos transmitidos desde la zona basal de la placa en flexión. Esto implica, que la contribución por flexura y por lo tanto la geometría asociada de la megafallas de subducción juega un rol importante durante escalas de tiempo del ciclo sísmico.

4. Mejorar la representación cinemática del proceso de subducción conduce a determinar de una forma robusta el grado de bloqueo en la megathrust y, por lo tanto, evaluar el déficit de deslizamiento y en consecuencia modelar adecuadamente la deformación intersísmica producida en el antearco.

# REFERENCIAS

Aagaard, B. T., Knepley, M. G., & Williams, C. A. 2013. A domain decomposition approach to implementing fault slip in finite-element models of quasi-static and dynamic crustal deformation. *J. geophys. res. solid earth*, **118**(6), 3059–3079.

Allmendinger, Richard W, Jordan, Teresa E, Kay, Suzanne M, & Isacks, Bryan L. 1997. ALTIPLANO-PUNA PLATEAU OF THE CENTRAL ANDES. *Annu. rev. earth planet. sci.*, **25**, 138–174.

Angermann, D., Klotz, J., & Reigber, C. 1999. Space-geodetic estimation of the Nazca-South America Euler vector. *Earth planet. sci*, **137**(3), 329–334.

Arancibia, Gloria, Cembrano, José, & Lavenu, Alain. 1999. Transpresión dextral y partición de la deformación en la Zona de Falla Liquiñe-Ofqui, Aisén, Chile (44-45ºS). *Rev. geológica chile*, **26**, 3–22.

Avouac, J.-P. 2015. From Geodetic Imaging of Seismic and Aseismic Fault Slip to Dynamic Modelling of the Seismic Cycle. *Annu. rev. earth planet. sci.*, **43**(1).

Bevis, Michael, Kendrick, Eric C., Smalley, Robert, Herring, Thomas, Godoy, Jorge, & Galban, Fernando. 2000. Crustal motion north and south of the Arica deflection: Comparing recent geodetic results from the central Andes. *Geochemistry, geophys. geosystems*, **1**(12), 1–10.

Bevis, Michael, Kendrick, Eric, Brooks, Benjamin, Allmendinger, Richard, & Isacks, Bryan. 2001. On the strength of interplate coupling and the rate of back arc convergence in the central Andes: An analysis of the interseismic velocity field. *Geochemistry, geophys. geosystems*, **2**.

Bloch, W., Schurr, B., Kummerow, J., Salazar, P., & Shapiro, S. A. 2018. From Slab Coupling to Slab Pull : Stress Segmentation in the Subducting Nazca Plate. *Geophys. res. lett.*, **45**(11), 5407–5416.

Bouchon, Michel, Marsan, David, Durand, Virginie, Campillo, Michel, Perfettini, Hugo, Madariaga, Raul, & Gardonio, Blandine. 2016. Potential slab deformation and plunge prior to the Tohoku, Iquique and Maule earthquakes. *Nat. geosci.*, **9**(apr), 380.

Brooks, Benjamin A, Bevis, Michael, Whipple, Kelin, Arrowsmith, J Ramon, Foster, James, Zapata, Tomas, Kendrick, Eric, Minaya, Estella, Echalar, Arturo, Blanco, Mauro, Euillades, Pablo, Sandoval, Mario, & Jr, Robert J Smalley. 2011. Orogenic-wedge deformation and potential for great earthquakes in the central Andean backarc. *Nat. geosci.*, **4**(5), 1–4.

Buffett, B. A. 2006. Plate force due to bending at subduction zones. *J. geophys. res.*, **111**(B9), B09405.

Buffett, B. A., & Rowley, D. B. 2006. Plate bending at subduction zones: Consequences for the direction of plate motions. *Earth planet. sci. lett.*, **245**, 359–364.

Bürgmann, Roland, Kogan, Mikhail G., Steblov, Grigory M., Hilley, George, Levin, Vasily E., & Apel, Edwin. 2005. Interseismic coupling and asperity distribution along the Kamchatka subduction zone. *J. geophys. res. solid earth*, **110**(7), 1–17.

Burov, E., & Guillou-Frottier, L. 2005. The plume head-continental lithosphere interaction using a tectonically realistic formulation for the lithosphere. *Geophys. j. int.*, **161**(2), 469–490.

Capitanio, F. A., & Morra, G. 2012. The bending mechanics in a dynamic subduction system: Constraints from numerical modelling and global compilation analysis. *Tectonophysics*, **522**, 224–234.

Cattin, R., Lyon-Caen, H., & Chéry, J. 1997. Quantification of interplate coupling in subduction zones and forearc topography. *Geophys. res. lett.*, **24**(13), 1563.

Cembrano, José, Schermer, Elizabeth, Lavenu, Alain, & Sanhueza, Alejandro. 2000. Contrasting nature of deformation along an intra-arc shear zone, the Liquiñeâ Ofqui fault zone , southern Chilean Andes. *Tectonophysics*, **319**, 129–149.

Charles, DeMets, Gordon, Richard G., Argus, Donald F., & Stein, Seth. 1994. Effect of recent revisions to the geomagnetic reversal time scale on estimates of current plate motions. *Geophys. res. lett.*, **21**(20), 2191–2194.

Chlieh, M., de Chabalier, J. B., Ruegg, J. C., Armijo, R., Dmowska, R., Campos, J., & Feigl, K. L. 2004. Crustal deformation and fault slip during the seismic cycle in the North Chile subduction zone, from GPS and InSAR observations. *Geophys. j. int.*, **158**(2), 695–711.

Chlieh, M., Avouac, J. P., Sieh, K., Natawidjaja, D. H., & Galetzka, J. 2008. Heterogeneous coupling of the Sumatran megathrust constrained by geodetic and paleogeodetic measurements. *J. geophys. res. solid earth*, **113**.

Chlieh, Mohamed, Perfettini, Hugo, Tavera, Hernando, Avouac, Jean-Philippe, Remy, Dominique, Nocquet, Jean-Mathieu, Rolandone, Frédérique, Bondoux, Francis, Gabalda, Germinal, & Bonvalot, Sylvain. 2011. Interseismic coupling and seismic potential along the Central Andes subduction zone. *J. geophys. res.*, **116**(B12), B12405.

Čížková, Hana, van Hunen, Jeroen, & van den Berg, Arie. 2007. Stress distribution within subducting slabs and their deformation in the transition zone. *Phys. earth planet. inter.*, **161**(3-4), 202 214.

Cohen, Steven C. 1994. Evaluation of the Importance of Model Features For Cyclic Deformation Due to DipâSlip Faulting. *Geophys. j. int.*, **119**(3), 831–841.

Conrad, C. P., Bilek, S., & Lithgow-Bertelloni, C. 2004. Great earthquakes and slab pull: Interaction between seismic coupling and plate-slab coupling. *Earth planet. sci. lett.*, **218**, 109–122.

Contreras, M., Tassara, A., Gerbault, M., Araya, R., & Bataille, K. 2016. Interseismic deformation at subduction zones investigated by 2D numerical modeling: case study before the 2010 Maule earthquake. *Andean geol.*, **43**(3), 247–262.

Dorbath, C., Gerbault, M., Carlier, G., & Guiraud, M. 2008. Double seismic zone of the Nazca plate in northern Chile: High-resolution velocity structure, petrological implications, and thermomechanical modeling. *Geochemistry, geophys. geosystems*, **9**(7).

Douglass, J. J., & Buffeft, B A. 1995. The stress state implied by dislocation models of. *Geophys. res. lett.*, **22**(23), 3115–3118.

Dragert, H., Wang, K., & James, T. S. 2001. A silent slip event on the deeper Cascadia subduction interface. *Science (80-. ).*, **292**(5521), 1525–1528.

Du, Y., A., Aydin, & P., Segall. 1992. Comparison of various inversion techniques as applied to the determination of a geophysical deformation model for the 1983 Borah Peak earthquake. *Seism. soc. am.*, **82**(4), 1840–1866.

Faccenda, M., & Mancktelow, N.S. 2010. Fluid flow during unbending: Implications for slab hydration, intermediate-depth earthquakes and deep fluid subduction. *Tectonophysics*, **149**(1-2), 149–154.

Forsyth, D.W., & Uyeda, S. 1975. On the relative importance of the driving forces of plate motion. *Geophys. j. r. astron. soc.*, **43**, 162–200.

Fourel, L., Goes, S., & Morra, G. 2014. The role of elasticity in slab bending. *Geochemistry, geophys. geosystems*, **15**(11), 4692–4711.

Gerbault, M., Cembrano, J., Mpodozis, C., Farias, M., & Pardo, M. 2009. Continental margin deformation along the Andean subduction zone: Thermo-mechanical models. *Phys. earth planet. inter.*, **177**, 180–205.

Gutscher, Marc-Andre, Spakman, W., & Engdahl, E Robert. 2000. Geodynamics of flat subduction: tomographic constraints from the Andean margin Cocos. *October*, **19**(5), 814–833.

Hager, B. H. 1984. Subducted slabs and the geoid: constraints on mantle rheology and flow. *J. geophys. res.*, **89**, 6003–6015.

Hashimoto, M., & Jackson, D. 1993. Plate tectonics and crustal deformation around the Japanese Islands. *J. geophys. res.*, **98**, 16149.

Hassani, R., Jongmans, D., & Chéry, J. 1997. Study of plate deformation and stress in subduction processes using two-dimensional numerical models. *J. geophys. res.*, **102**, 17951.

Ho-Le, K. 1988. Finite element mesh generation methods: a review and classification. *Comput. des.*, **20**(1), 27–38.

Hu, Y, Wang, K, He, J, Klotz, J, & Khazaradze, G. 2004. Three-dimensional viscoelastic finite element model for postseismic deformation of the great 1960 Chile earthquake. *J. geophys. res.*, **109**(B12403).

Hyodo, Mamoru, & Hirahara, Kazuro. 2003. A viscoelastic model of interseismic strain concentration in Niigata-Kobe Tectonic Zone of central Japan. *Earth, planets sp.*, **55**(11), 667–675.

Jara, J., Socquet, A., & Marsan D. & Bouchon, M. 2017. Long-term interactions between intermediate depth and shallow seismicity in North Chile subduction zone. *Geophys. res. lett.*, **44**, 9283–9292.

Jarrard, Richard D. 1986. Relations among subduction parameters. *Rev. geophys.*, **24**(2), 217–284.

Kanda, R. V. S., & Simons, M. 2010. An elastic plate model for interseismic deformation in subduction zones. *J. geophys. res.*, **115**(B3), B03405.

Khazaradze, G. 2002. Prolonged post-seismic deformation of the 1960 great Chile earthquake and implications for mantle rheology. *Geophys. res. lett.*, **29**(22), 2050.

Khazaradze, G., & Klotz, J. 2003. Short-and long-term effects of GPS measured crustal deformation rates along the south central Andes. *J. geophys. res. solid earth*, **108**(B6).

Klotz, Jürgen, Khazaradze, Giorgi, Angermann, Detlef, Reigber, Christoph, Perdomo, Raul, & Cifuentes, Oscar. 2001. Earthquake cycle dominates contemporary crustal deformation in Central and Southern Andes. *Earth planet. sci. lett.*, **193**(3-4), 437–446.

Lamb, S. 2006. Shear stresses on megathrusts: Implications for mountain building behind subduction zones. *J. geophys. res.*, **111**(B7).

Lay, T., Ammon, C. J., Kanamori, H., Koper, K. D., Sufri, O., & Hutko, a. R. 2010. Teleseismic inversion for rupture process of the 27 February 2010 Chile (M w 8.8) earthquake. *Geophys. res. lett.*, **37**(13), n/a–n/a.

Li, Z.H., Leo, Di, J.F., Ribe, & N.M. 2014. Subductionâinduced mantle flow, finite strain, and seismic anisotropy: Numerical modeling. *J. geophys. res.*, **119**(6), 5052–5076.

Lorito, S., Romano, F., Atzori, S., Tong, X., Avallone, a., McCloskey, J., Cocco, M., Boschi, E., & Piatanesi, a. 2011. Limited overlap between the seismic gap and coseismic slip of the great 2010 Chile earthquake. *Nat. geosci.*, **4**(3), 173–177.

Loveless, John P, & Meade, Brendan J. 2010. Geodetic Imaging of Plate Motions , Slip Rates , and Partitioning of Deformation in Japan. *J. geophys. res.*, **115**(B02410).

Marone, C. 1998. Laboratory-derived friction laws and their application to seismic faulting. *Earth planet. sci*, **26**, 643–646.

Mazzotti, S., Le Pichon, X., Henry, P., & Miyazaki, S.-I. 2000. Full interseismic locking of the Nankai and Japan-west Kurile subduction zones: An analysis of uniform elastic strain accumulation in Japan constrained by permanent GPS. *J. geophys. res. solid earth*, **105**(B6), 13159–13177.

Melosh, H. J., & Raefsky, A. 1981. Asimple and efficient method for introducing faults intofinite element computations,. *Bull. seismol. soc. am.*, **71**(5), 1391–1400.

Métois, M, Socquet, Anne, Vigny, C, Métois, M, Socquet, Anne, & Interseismic, C Vigny. 2012. Interseismic coupling , segmentation and mechanical behavior of the Central Chile subduction zone. *J. geophys. res.*, **117**(B03406).

Métois, M., Socquet, A., Vigny, C., Carrizo, D., Peyrat, S., Delorme, A., Maureira, E., & Ortega, I. 2013. Revisiting the North Chile seismic gap segmentation using GPS-derived interseismic coupling. *Geophys. j. int.*, **194**, 1283–1294.

Moreno, M, Klotz, J, Melnick, D, Echtler, H, & Bataille, K. 2008. Active faulting and heterogeneous deformation across a megathrust segment boundary from GPS data, south central Chile (36â39 Â° S). *Geochemistry, geophys. geosystems*, **9**(November).

Moreno, M., Rosenau, M., & Oncken, O. 2010. 2010 Maule earthquake slip correlates with pre-seismic locking of Andean subduction zone. *Nature*, **467**(7312), 198–202.

Moreno, M, Melnick, D, Rosenau, M, Bolte, J, Klotz, J, Echtler, H, Baez, J, Bataille, K, & Chen, J. 2011. Heterogeneous plate locking in the South-Central Chile subduction zone : Building up the next great earthquake. *Earth planet. sci. lett.*, **305 (3-4)**, 413–424.

Moreno, M., Melnick, D., Rosenau, M., Baez, J., Klotz, J., Oncken, O., Tassara, A., Chen, J., Bataille, K., Bevis, M., Socquet, A., Bolte, J., Vigny, C., Brooks, B., Ryder, I., Grund,

V., Smalley, B., Carrizo, D., Bartsch, M., & Hase, H. 2012. Toward understanding tectonic control on the Mw 8.8 2010 Maule Chile earthquake. *Earth planet. sci. lett.*, **321-322**, 152–165.

Norabuena, E., L., Leffler-griffin, Mao, A., Dixon, T., Stein, S., Sacks, I ., Ocola, L., & Ellis, M. 1998. Space Geodetic Observations of Nazca-South America Convergence Across the Central Andes. *Science (80-. ).*, **279**.

Okada, Y. 1985. Surface deformation due to shear and tensile faults in a half-space. *Bull. seismol. soc. am.*, **75**(4), 1135–1154.

Okada, Yoshimitsu. 1992. *Internal deformation due to shear and tensile faults in a half space.pdf*.

Oleskevich, D. A., Hyndman, R. D., & Wang, K. 1999. The updip and downdip limits to great subduction earthquakes : Thermal and structural models of Cascadia , South Alaska , SW Japan , and Chile. *J. geophys. res.*, **104**, 14,965–14,991.

Perfettini, Hugo, Avouac, Jean-Philippe, Tavera, Hernando, Kositsky, Andrew, Nocquet, Jean-Mathieu, Bondoux, Francis, Chlieh, Mohamed, Sladen, Anthony, Audin, Laurence, Farber, Daniel L, & Others. 2010. Seismic and aseismic slip on the central Peru megathrust. *Nature*, **465**(7294), 78–81.

Piromallo, C., Becker, T.W., Funiciello, F., & Faccenna, C. 2006. Three dimensional instantaneous mantle flow induced by subduction. *Geophys. res. lett.*, **33**(8).

Poliakov, A., & Podladchikov, Y. 1992. Diapirism and topography. *Geophys. j. int.*, **109**(3), 553–564.

Prawirodirdjo, L., Bocl, Y., McCaffrey, R., Genrich, J, Calais, E., Stevens, C., Puntodewo, S., Subarya, C., Rais, J., Zwick, P., & Others. 1997. Geodetic observations of interseismic strain segmentation at the Sumatra subduction zone. *Geophys. res. lett.*, **24**(21), 2601–2604.

Provost, A.-S., & Chery, J. 2006. Relation between effective friction and fault slip rate across the Northern San Andreas fault system. *Geol. soc. london, spec. publ.*, **253**, 429–436.

Ribe, N. M. 2010. Bending mechanics and mode selection in free subduction: a thin-sheet analysis. *Geophys. j. int.*, **180**(2), 559–579.

Ruegg, J.C., Rudloff, A., Vigny, C., Madariaga, R., de Chabalier, J.B., Campos, J., Kausel, E., Barrientos, S., & Dimitrov, D. 2009. Interseismic strain accumulation measured by GPS in the seismic gap between Constitución and Concepción in Chile. *Phys. earth planet. inter.*, **175**(1-2), 78–85.

Savage, J. C. 1983. A Dislocation Model of Starins Accumulation and Release at Subduction Zone. *J. geophys. res.*, **88**(3), 4984–4996.

Schellart, W. P. 2009. Evolution of the slab bending radius and the bending dissipation in three-dimensional subduction models with a variable slab to upper mantle viscosity ratio. *Earth planet. sci. lett.*, **288**(1), 309–319.

Scholz, C H. 1998. Earthquakes and friction laws. *Nature*, **391**(6662), 37–42.

Scholz, C. H. 2002. *The mechanics of earthquakes and faulting*. Cambridge university press.

Schurr, Bernd, Günter, Asch, Sebastian, Hainzl, Jonathan, Bedford, Andreas, Hoechner, Mauro, Palo, Rongjiang, Wang, Moreno, Marcos, Bartsch, Mitja, Zhang, Yong, Oncken, Onno, Tilmann, Frederik, Dahm, Torsten, Victor, Pia, Barrientos, Sergio, & Vilotte, Jean-pierre. 2014. Gradual unlocking of plate boundary controlled initiation of the 2014 Iquique earthquake. *Nature*, **512**, 299–302.

Smith, D., & Turcotte, D. 1993. *Contributions of space geodesy to geodynamics: earth dynamics*. Vol. 2. American Geophysical Union.

Sobolev, S.V., & Babeyko, A.Y. 2005. What drives orogeny in the Andes? *Geology*, **33**(8), 617–620.

Tassara, A. 2010. Control of forearc density structure on megathrust shear strength along the Chilean subduction zone. *Tectonophysics*, **495**(1-2), 34–47.

Tassara, A., & Echaurren, A. 2012. Anatomy of the Andean subduction zone: Three-dimensional density model upgraded and compared against global-scale models. *Geophys. j. int.*, **189**, 161–168.

Thatcher, W., & Rundle, J. B. 1984. A viscoelastic coupling model for the cyclic deformation due to periodically repeated Earthquakes at subduction zones. *J. geophys. res.*, **89**, 7631.

Tong, Xiaopeng, Sandwell, David, Luttrell, Karen, Brooks, Benjamin, Bevis, Michael, Shimada, Masanobu, Foster, James, Smalley, Robert, Parra, Hector, Báez Soto, Juan Carlos, Blanco, Mauro, Kendrick, Eric, Genrich, Jeff, & Caccamise, Dana J. 2010. The 2010 Maule, Chile earthquake: Downdip rupture limit revealed by space geodesy. *Geophys. res. lett.*, **37**(24), n/a–n/a.

Turcotte, D. L., & Schubert, G. 2002. *Geodynamics*. University Press.

Van Dinther, Y., Gerya, T. V., Dalguer, L. A., Mai, P. M., Morra, G., & Giardini, D. 2013. The seismic cycle at subduction thrusts: Insights from seismo-thermo- mechanical models. *J. geophys. res. solid earth*, **118**, 6183–6202.

Wang, Kelin. 2007. Elastic and Viscoelastic Models of Crustal Deformation in Subduction Earthquake Cycles. *Columbia univ. press. new york*, 1–46.

Wang, Kelin, Wells, Ray, Mazzotti, Stephane, Hyndman, Roy D., & Sagiya, Takeshi. 2003. A revised dislocation model of interseismic deformation of the Cascadia subduction zone. *J. geophys. res. solid earth*, **108**(B1).

Wang, Kelin, Hu, Yan, & He, Jiangheng. 2012. Deformation cycles of subduction earthquakes in a viscoelastic Earth. *Nature*, **484**(7394), 327–332.

Zhao, S., & Takemoto, S. 2000. Deformation and stress change associated with plate interaction at subduction zones : a kinematic modelling. *Geophys. j. int.*, 300–318.

**Apéndice A**

# Anexo I : Formulación de elementos finitos de la ecuación de elasticidad

La solución numérica de una Ecuación Diferencial Parcial (PDE) puede ser obtenida aplicando el método de Galerkin, este es un método residual ponderado que comienza con una estimación de la solución y exige que se minimice su error promedio ponderado.

Se considera el caso general de una ecuación diferencial : $Lu = f$, en donde se prueba una solución aproximada de la forma $\widetilde{u} = \sum_{i=1}^{N} \phi_i u_i$, donde $\phi_i$ son funciones de prueba (entradas) y $u_i$ son cantidades desconocidas que necesitamos evaluar. Además la solución debe satisfacer las condiciones de contorno de Dirichlet.

Puesto $\widetilde{u} = \sum_{i=1}^{N} \phi_i u_i$ es una aproximación, al substituir en la ecuación inicial resultará un error $\widetilde{\epsilon}$ a minizar :

$$L\widetilde{u} = f + \widetilde{\epsilon}$$

$$\widetilde{\epsilon} = L\widetilde{u} - f$$

tal que :

$$\int_V \phi(L\widetilde{u} - f)dV = 0$$

Comenzamos con la ecuación de elasticidad (forma fuerte) con :

1) una solución de prueba, $\vec{u}$, que es un campo vectorial diferenciable por piezas y satisface las condiciones de contorno de Dirichlet en $S_u$

2) la función de ponderación, $\vec{\phi}$, que es un campo vectorial diferenciable por partes y es cero en $S_u$

$$\sigma_{ij,j} + f_i = 0 \text{ en } V, \tag{A.0.1}$$

$$\sigma_{ij} n_j = T_i \text{ sobre } S_T, \tag{A.0.2}$$

$$u_i = u_i^o \text{ sobre } S_u, \tag{A.0.3}$$

$$R_{ki}(u_i^+ - u_i^-) = d_k \text{ sobre } S_f, \text{ y} \tag{A.0.4}$$

$$\sigma_{ij} = \sigma_{ji} \text{ (simétrico).} \tag{A.0.5}$$

Construimos la forma débil, calculando el producto punto entre la ecuación de elasticidad y la función de ponderación $\phi_i$ , estableciendo la integral sobre el dominio a cero:

$$\int_V (\sigma_{ij,j} + f_i)\, \phi_i \, dV = 0, \text{ or} \tag{A.0.6}$$

$$\int_V \sigma_{ij,j} \phi_i \, dV + \int_V f_i \phi_i \, dV = 0. \tag{A.0.7}$$

Considere el teorema de divergencia aplicado al producto de punto del tensor de tensión y la función de ponderación, $\sigma_{ij}\phi_i$,

$$\int_V (\sigma_{ij}\phi_i)_{,j} \, dV = \int_S (\sigma_{ij}\phi_i) n_i \, dS. \tag{A.0.8}$$

Expandimos el miembro del lado izquierdo

$$\int_V \sigma_{ij,j}\phi_i \, dV + \int_V \sigma_{ij}\phi_{i,j} \, dV = \int_S \sigma_{ij}\phi_i n_i \, dS, \text{ or} \tag{A.0.9}$$

$$\int_V \sigma_{ij,j}\phi_i \, dV = -\int_V \sigma_{ij}\phi_{i,j} \, dV + \int_S \sigma_{ij}\phi_i n_i \, dS. \tag{A.0.10}$$

La sustitución en la forma débil da

$$-\int_V \sigma_{ij}\phi_{i,j}\,dV + \int_S \sigma_{ij}\phi_i n_i\,dS + \int_V f_i\phi_i\,dV = 0. \tag{A.0.11}$$

Volviendo nuestra atención al segundo término, separamos la integración sobre S en la integración sobre $S_T$ y $S_u$ (vamos a considerar tracciones sobre la superficie de falla, $S_f$, asociado con el modelo constitutivo de falla en la sección **??**),

$$-\int_V \sigma_{ij}\phi_{i,j}\,dV + \int_{S_T} \sigma_{ij}\phi_i n_i\,dS + \int_{S_u} \sigma_{ij}\phi_i n_i\,dS + \int_V f_i\phi_i\,dV = 0, \tag{A.0.12}$$

y reconocer que

$$\sigma_{ij}n_i = T_i \text{ on } S_T \text{ and} \tag{A.0.13}$$

$$\phi_i = 0 \text{ on } S_u, \tag{A.0.14}$$

para que la ecuación se reduzca a

$$-\int_V \sigma_{ij}\phi_{i,j}\,dV + \int_{S_T} T_i\phi_i\,dS + \int_V f_i\phi_i\,dV = 0. \tag{A.0.15}$$

Expresamos la solución de prueba y la función de ponderación como combinaciones lineales de funciones de base,

$$u_i = \sum_m a_i^m N^m, \tag{A.0.16}$$

$$\phi_i = \sum_n c_i^n N^n. \tag{A.0.17}$$

Teniendo en cuenta que debido a que la solución de prueba satisface la condición de contorno de Dirichlet, el número de funciones de base para $u$ es generalmente mayor

que el número de funciones de base para $\phi$, i.e., $m > n$. La sustitución de las expresiones de la solución de prueba y de la función de ponderación da :

$$-\int_V \sigma_{ij} \sum_n c_i^n N_{,j}^n \, dV + \int_{S_T} T_i \sum_n c_i^n N^n \, dS + \int_V f_i \sum_n c_i^n N^n \, dV = 0, \text{ or} \tag{A.0.18}$$

$$\sum_n c_i^n \left( -\int_V \sigma_{ij} N_{,j}^n \, dV + \int_{S_T} T_i N^n \, dS + \int_V f_i N^n \, dV \right) = 0. \tag{A.0.19}$$

Debido a que la función de ponderación es arbitraria, esta ecuación debe contener para todos los $c_i^n$, de modo que la cantidad entre paréntesis sea cero para cada $c_i^n$

$$-\int_V \sigma_{ij} N_{,j}^n \, dV + \int_{S_T} T_i N^n \, dS + \int_V f_i N^n \, dV = \vec{0}. \tag{A.0.20}$$

Queremos resolver esta ecuación para los coeficientes desconocidos $a_i^m$ sujeto a

$$u_i = u_i^o \text{ on } S_u, \text{ y} \tag{A.0.21}$$

$$R_{ki}(u_i^+ - u_i^-) = d_k \text{ sobre } S_f, \tag{A.0.22}$$

# Índice de figuras